STRESS CORROSION CRACKING OF 316 STAINLESS STEEL IN CAUSTIC SOLUTIONS

by

DAVID CHARLES CROWE

B.Sc., (Mechanical Engineering),

The University of Manitoba, 1977

A THESIS SUBMITTED IN PARTIAL FULFILMENT OF

THE REQUIREMENTS FOR THE DEGREE OF

MASTER OF APPLIED SCIENCE

in

THE FACULTY OF GRADUATE STUDIES

Department of Metallurgical Engineering

We accept this thesis as conforming

to the required standard

THE UNIVERSITY OF BRITISH COLUMBIA

May 1982

In presenting this thesis in partial fulfilment of the requirements for an advanced degree at the University of British Columbia, I agree that the Library shall make it freely available for reference and study. I further agree that permission for extensive copying of this thesis for scholarly purposes may be granted by the head of my department or by his or her representatives. It is understood that copying or publication of this thesis for financial gain shall not be allowed without my written permission.

Department of Metallurgical Engineering

The University of British Columbia
2075 Wesbrook Place
Vancouver, Canada
V6T 1W5

Date 1 May 1982

ABSTRACT

Stress corrosion cracking (SCC) of type 316 stainless steel was studied in hot (92°C) solutions of 3.35 mol/kg NaOH and 2.5 mol/kg NaOH + 0.423 mol/kg Na_2S by means of potentiostatically controlled slow strain rate testing techniques (SSRT). Anodic polarization curves were also determined for the steel, together with those for Ni, Cr and Fe. SCC occurred in the transpassive region in 3.35 mol/kg NaOH, with no detectable tendency to crack in the active-passive region, unless in the sensitized condition. In the NaOH + Na_2S solution, SCC was detected in the active-passive region.

Fracture mechanics techniques were used to study the kinetics of stress corrosion crack propagation in 3.35, 8 and 12 mol/kg NaOH, and 12 mol/kg NaOH + 0.423 mol/kg Na_2S. Cracking was studied as a function of stress intensity (K_I), temperature (T) and potential (E). Crack fractography was studied by scanning electron microscopy and corrosion films investigated by electron diffraction. Region I (K_I-dependent) and Region II (K_I-independent) crack behavior were observed.

The results indicated that SCC was associated with potentials at which instabilities occurred in passive films and that the basic mechanism of cracking involved a film rupture and dissolution process, with dissolution processes

exerting predominant rate control in Region II. In the case of the sulfide containing solution, hydrogen embrittlement processes could not be eliminated as a contributing factor.

TABLE OF CONTENTS

LIST OF TABLES

LIST OF FIGURES

LIST OF SYMBOLS AND ABBREVIATIONS

Symbol	
a	crack length
a_o	lattice parameter
d	crystal d-spacing
D	diameter of diffraction pattern ring
E	electrochemical potential
E_{CORR}	corrosion potential
F	Faraday (9.85×10^4 A·s)
h,k,l	Miller indices
i_a	anodic current density
κ	camera constant for electron diffraction
K_I	stress intensity for mode I opening
K_{ISCC}	threshold stress intensity
P	load
Q	apparent activation energy
ρ	density
R	gas constant (8.314 kJ/mol deg)
r_y	plastic zone size
σ_y	yield stress
T	temperature °K
$\dot{v}$	crack velocity
V_{SHE}	volts with respect to the standard hydrogen electrode

V_{SCE}	volts with respect to the standard calomel electrode
W	equivalent weight

Abbreviation

SCC	stress corrosion cracking
SSRT	slow strain rate test
TN-DCB	T-notch double cantilever beam

ACKNOWLEDGEMENT

I am indebted to my research supervisor, Desmond Tromans, for his unfailing encouragement and patience.. The staff has also been very generous in helping me. L. Frederick, R. MacLeod, E. Klassen, M. Mager, H. Tump, E. Armstrong and K. Kent deserve special thanks.

My parents have given me a great amount of understanding and support throughout this work.

Financial support has been provided by Alcan as a fellowship which I received for two years. Additional support was provided by the National Science and Engineering Research Council. Their contributions have been gratefully received.

1. INTRODUCTION

Stress corrosion cracking (SCC) is a time dependent failure process caused by the conjoint action of a tensile stress and corrosion. It occurs in many different alloy-environment combinations and is of particular concern in industrial situations wherever steels are exposed to hot, caustic solutions. Such steels include type 316 austenitic stainless steel, which is the subject of this thesis.

Sodium hydroxide solutions are used in a variety of chemical processes such as wood pulping, alumina production, or alkalinization of chemical process streams. Unwanted caustic deposits also build up in crevices or splash zones in boilers, tanks or other equipment where pH control is practiced. The effects of caustic solutions have been investigated extensively and a better understanding has developed hand in hand with better techniques of investigation.

Several techniques have been employed for study of SCC. Early studies of stress corrosion of stainless steel in caustic solutions were done using loaded tensile specimens[1] or pressurized tube specimens.[1-3] U-bend specimens and loaded longitudinal sections of pipe also have been used.[4-7] In most of these tests the electrochemical potential was not measured or controlled. More recently, straining electrode[8,9]

or slow strain rate testing has been employed.[10,11] The slow strain rate test has been used primarily as a relatively rapid test for determining potential regions for susceptibility to SCC. Another recent method employs fracture mechanics specimens to allow study of growth of a crack of well characterized geometry.[12-15] The crack growth rate is related to the stress intensity, K_I, at the crack tip. Time required for crack initiation is minimized.

Studies of SCC of stainless steels in caustic solutions have shown that several variables are important. These include temperature, composition and concentration of the environment, electrochemical potential, alloy composition, thermomechanical effects, and stress intensity. Much of the present knowledge of SCC in Fe-Cr-Ni alloys has been summarized in several reviews.[16-21]

1.1 Temperature

The effect of temperature was investigated systematically by Snowden[3] who showed that time-to-failure of specimens increased dramatically as the temperature was decreased. Agrawal and Staehle also observed this.[22]

1.2 Electrochemical Potential

The importance of electrochemical potential to SCC was

not studied until recently. Theus,[7] in a study of Inconel 600, Incoloy 800 and type 304, observed that the 304 stainless steel cracked if the potential was more than 30 mV above the open circuit corrosion potential. Morris has investigated the potential dependence of SCC of Alloy 600.[23]

Park et al.[8] in a study of 304 stainless steel straining electrodes in boiling 20 N NaOH, found a short time-to-failure near the corrosion potential, no failure in the passive region, failure times decreasing in the primary transpassive region and very short time to failure in the secondary passive region.

Dahl et al.[24] found that in 20% NaOH at 225°C, 18 Cr-9Ni stainless steel was susceptible to cracking at the active anodic current peak and at cathodic currents.

Long et al.[25] and Agrawal et al.[26] have conducted polarization studies of Fe-Cr-Ni alloys in NaOH solutions to gain a better understanding of how the polarization behavior of the alloy is affected by that of its constituents.

Okada et al.[27] quoted unpublished work by Subramanyam and Staehle which indicated that the potential affected the cracking mode. It was intergranular at the transpassive potential and transgranular at the active-passive potentials

for 304 stainless steel in 70% NaOH. Park et al.[8] observed that cracking mode was a function of potential.

1.3 Composition and Concentration of the Enviornment

Higher concentrations of NaOH have been shown to reduce time-to-failure.[3,7,22] The concentration of caustic was observed to affect the fractography, changing it from intergranular to mixed intergranular-transgranular in 304 stainless steel as the NaOH concentration was increased.[2,28]

The addition of other species to the solution may shift the free corrosion potential.[9,29,30] In this way many additives may inhibit corrosion by shifting the free corrosion potential into a region where there is no susceptibility to SCC. Park et al.[9,29] concluded that the inhibitors they tested shift the free corrosion potential for 304 stainless steel in a noble direction in 20 N NaOH. Early observations of inhibitors did not consider this effect on potential.[3]

Addition of sulfur to simulated white liquor (NaOH + Na_2S solution) has been shown to shift the free corrosion potential for mild steel.[31] More sulfur is needed as the $Na_2S_2O_3$ concentration is increased.[32] Polysulfide acts as a passivating inhibitor for mild and stainless steels.[33]

Theus and Staehle[17] have observed that sulfide may affect the fracture mode. They quoted work on 304 stainless steel[34] in 50% NaOH with 0.03 mol/liter Na_2S at 180°C in which intergranular cracking was observed. In other work with 50% NaOH at higher temperature, transgranular cracking was observed.

The fractography was also observed to change when KOH was used instead of NaOH.[2]

NaCl has been observed to increase the time-to-failure for 321 stainless steel in 3% NaOH.[35]

1.4 Alloy Composition

The effect of composition of the alloy has been investigated.[1] Increasing amounts of chromium in the alloy improved resistance to SCC in 50% NaOH at 300 °C. At 10-15% chromium, a higher nickel content also was found to be beneficial but the still higher nickel content used with 20-25% chromium reduced resistance to cracking.

McIlree and Michels[6] found that in deaerated 50% NaOH at 300 °C, nickel increased the resistance to SCC but in an aerated 50% NaOH solution both high chromium and high nickel content were necessary to increase SCC resistance. Potential

was not measured or controlled.

The influence of nickel has been investigated thoroughly in $MgCl_2$ solutions.[36,37] Copson[36] produced a curve relating nickel content to time-to-failure in $MgCl_2$. A minimum time-to-failure occurred for about 8% nickel. Speidel[13] observed for stainless steel in NaCl solution at 105 °C that the Copson curve is reproduced by plotting the stress corrosion threshhold stress intensity (K_{ISCC}) versus nickel content in a stainless steel of ~ 18% chromium. K_{ISCC} is the stress intensity below which cracking is not detected. Sedriks et al.[4] found that K_{ISCC} increased with increasing nickel content for stainless steel in NaOH solutions. As the nickel content was increased the crack path changed from transgranular to intergranular.

The amount of nickel and chromium in the alloy has been identified as important in the stainless overlay used in kraft pulp digesters. Crooks and Linnert[38] attributed overlay corrosion to attack of small areas of low alloy content dispersed throughout the overlay lining and frequently a low average level of alloying elements in the lining. Martensite was observed in places where alloy content was below approximately 13% chromium and 8% nickel. Rapid attack occurred there.

Other studies have considered the effect of carbon,[39,40]

molybdenum,[1,6,39,41] silicon,[42] aluminum,[43] and phosphorus.[40]

1.5 Thermomechanical Effects

Sensitization (i.e. carbide precipitation) occurs when the alloy is heated in the range 500 to 800 °C. Carbides are formed at the grain boundaries, and these produce a continuous chromium denuded path for intergranular corrosion.[44] The effect of sensitization on SCC of stainless steel in NaOH solutions has been investigated. Wilson and Aspden[5] concluded that sensitization is not damaging to 304 stainless steel in 10% NaOH at 316 °C and 332 °C or in 50% NaOH at 316 °C. Wilson et al.[39] found that for 304 stainless steel in 50% NaOH at 371 °C sensitization had no effect on cracking. It also had no effect on the life of 316L or 316 stainless steel in 10% NaOH at 316 °C. In both cases cracking was transgranular. They concluded that grain boundary carbides per se did not induce susceptibility in 10-50% NaOH at 149-371 °C. Also, they found that in 10% NaOH at 316 °C the 304 stainless steel was resistant to SCC but type 316 was not.

The effect of cold work has also been investigated.[6,45] Cold work may induce partial martensitic transformation.[46] Asaro et al.[47] identified martensite formation with transgranular SCC of 304 stainless steel in hot caustic solutions. McIlree and Michels[6] obtained evidence that stress relief of

304 stainless steel for four hours at 593 °C did not improve resistance in 50% NaOH at 294 and 332 °C. Wilson and Aspden[45] found that cold rolling had no effect on the cracking of 304 and 304L stainless steel in both 10% and 50% NaOH.

Grain size was found to have no effect on failure time.[39]

1.6 Stress Intensity

The influence of stress intensity on cracking rate of stainless steel in hydroxide solutions has not been examined even though it has been shown to be important in other systems.[12-14, 48,49]

1.7 Mechanisms of SCC

In the research described in the literature, the variables in the stress corrosion process have not been fully controlled or defined. In particular, the potential may not have been measured or controlled; only recently has its importance been recognized. Within these limitations, several mechanisms have been proposed to account for the cracking process. These mechanisms have been essentially qualitative rather than quantitatively predictive.

Most mechanistic descriptions of SCC in caustic environments have centered on the film rupture and dissolution

mechanism. This has been described by Staehle.[21] According to this model, a protective surface film is ruptured by slip steps. Localized dissolution occurs at the newly exposed surface until repassivation is complete, with the amount of dissolution occurring before repassivation influencing the geometry of the attacked area. Subsequent film rupture and dissolution cycles at the localized area constitute cracking. In this model, the cracking rate is related to the dissolution rate and time spent in the dissolution stage. Film instability in various potential ranges and transient dissolution currents are the principal factors in determining susceptibility. In some instances the detailed dissolution morphology of crack propagation is believed to arise via tunneling at the crack tip.[21,50]

Vermilyea[51] has formulated a detailed film rupture model in which the crack advances by dissolution before repassivation occurs. Further dissolution would occur when the surface film is ruptured again. Diegle and Vermilyea[52] have presented evidence that the ratio of crack tip corrosion rate to crack tip strain rate must exceed a critical value, depending on the strain gradient ahead of the crack tip, to promote SCC of steel in NaOH.

Scully[53] has described a model for dissolution controlled cracking, requiring a critical delay in repassivation time

during which dissolution occurs. In a later paper,[54] Scully has quoted work by Newman[55] showing that the charge passed during the repassivation event fitted the analysis of cracking in a Cr-Mo steel exposed to 8M NaOH at 100 °C. Scully has noted that Vermilyea's model may be more applicable to systems like steel in hydroxide solution where the crack tip solution may not be much different than the bulk solution and commented that evidence about the crack tip solution composition is surprisingly lacking.

Park et al.[8] using a high strain rate loading technique where the surface was ruptured, have related the SCC susceptibility of stainless steel in hydroxide solution to the ratio of current on a bare metal surface to that on a filmed electrode. Their work supported the film rupture and dissolution model.

Bignold[56] developed a model to explain the observed potential dependence of cracking rate and aspect ratio, and the existence of an anodic potential above which cracking ceases. His model is based on potential and current distributions in a crack. Doig and Flewitt[57] have also considered the distribution of potential in a stress corrosion crack, and how this may affect crack propagation.

Very little quantitative information is available to

support or disprove the mechanisms suggested.

The role of hydrogen embrittlement in caustic SCC of stainless steels has been investigated by Holzworth.[58] The loss of ductility after cathodic charging was related to the amount of martensitic phases present. O'Brien and Seto[59] have studied the mechanism of hydrogen evolution at a stainless steel electrode in NaOH solution. They have tabulated reversible potentials, exchange current densities and Tafel slopes on 304L stainless steel for a range of NaOH concentrations. However no one has established that thermodynamic conditions exist within a crack under freely corroding conditions which could generate hydrogen and promote hydrogen embrittlement.

1.8 Present Objectives

The present investigation has employed improved techniques, particularly SSRT and fracture mechanics, to obtain new quantitative information on SCC in solutions of NaOH and solutions of NaOH with Na_2S added. The solution containing sulfide simulates white liquor wood-pulping solution used in the Kraft process.

During the experimental investigation the temperature, electrochemical potential, environment composition and

concentration, alloy composition, thermomechanical properties, and stress intensity have been controlled in order to provide quantitative data useful for understanding rate controlling mechanisms and for designing equipment.

2. EXPERIMENTAL

2.1 Polarization Curves

2.1.0 Introduction

Electrochemical reactions occur on metal electrodes when submersed in aqueous solution. The rate and direction of each reaction depends on the potential of the electrode.[60] To apply a potential different from that found under freely corroding conditions requires that current be supplied via an external circuit. In a potentiodynamic test, the potential (with respect to a standard reference electrode) is varied continuously through a range and this current is recorded. The record of the current versus potential is a polarization curve.[60] The curve may be used to obtain information on the reactions which take place on the surface.[25,26,60-62]

2.1.1 Materials and Preparation

Polarization curves were determined for five materials. Two AISI Type 316 stainless steels, pure iron, nickel and chromium were examined.

Type 316 stainless steel was received as 9.5 mm diameter rod and as 10.6 mm thick hot rolled, annealed and pickled plate. The compositions were determined by spectroscopic analysis, courtesy of CAE Machinery. Carbon content was determined separately by the more accurate LECO method. The results of the analyses are given in Table I.

Armco iron was received as 0.46 mm sheet. High purity vacuum arc nickel discs were 15 mm diameter and 6.5 mm thick. Purified carbon free fused chromium metal was in the form of irregular chunks less than 1 cm long.

Electrodes $\sim 1 cm^2$ in area were cut from each stock. A pure nickel wire was spot welded to each electrode and the wire was passed through 3 mm PTFE tubing. The electrode and tube were set in a disc of "Quickmount" selfsetting acrylic plastic. The electrode face, in its mounting, was polished to 600 grit, with final polishing being done on a clean paper with distilled water just before placing into the test cell.

The test cell, as shown schematically in Figure 1, was a 600 ml (polytetrafluorethylene) Teflon beaker fitted with a Teflon lid. The temperature of the solution was measured by a Teflon-coated thermistor temperature probe connected to

Table I Chemical Composition of Type 316 Steels

Rod Material										
	C	Mn	Si	Ni	Cr	Mo	P	S	Fe	
Batch 1	0.09	1.67	0.4	11.33	17.33	2.57	0.012	0.021	bal	wt%
Batch 2	0.09	1.69	0.38	11.52	16.6	2	0.014	0.014	bal	wt%

Plate Material										
	C	Mn	Si	Ni	Cr	Mo	P	S	Fe	
	0.09	1.75	0.38	10.29	15.7	2.0	0.015	0.015	bal	wt%

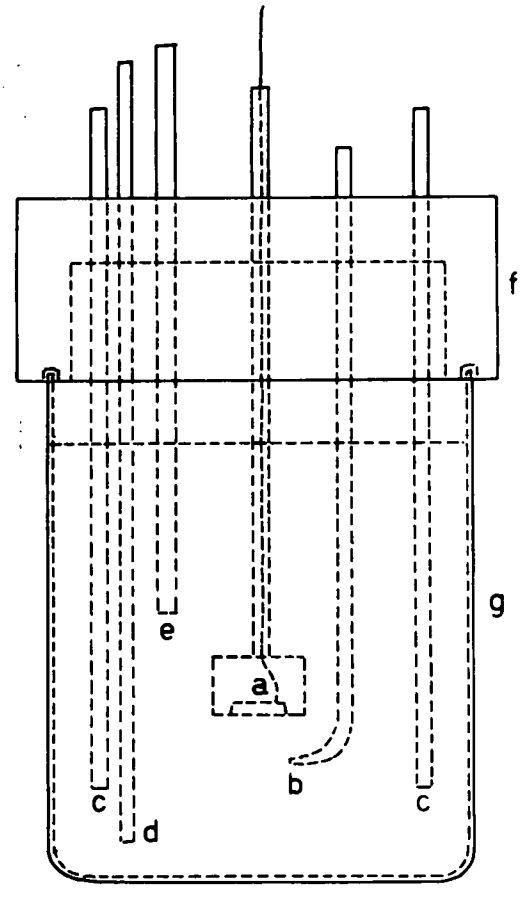

Figure 1: Test cell for polarization studies

a) test electrode (b) Luggin capillary

c) counter electrode (d) temperature probe

e) nitrogen purge (f) lid

g) beaker.

a temperature controller. The controller regulated the current to a heating mantle in which the test cell was enclosed. Temperature was regulated to within $\pm$ 1 °C. Two graphite counter electrodes, the working electrode and the Luggin capillary reference electrode were inserted through the lid. There were openings in the lid for the temperature probe, reflux condenser, Teflon coated thermometer, and nitrogen purge line. The Teflon Luggin capillary contained a cotton thread and was filled with saturated (at 24 °C) KCl solution. The cotton thread minimized vapor bubble formation. The Luggin capillary connected via a saturated KCl saltbridge to an external standard calomel electrode at 24°°C.

The solutions were made with reagent grade NaOH pellets and $Na_2S \cdot 9H_2O$ hydrate. Distilled water was employed which was first boiled and purged with USP nitrogen before adding the chemicals. The purge was continued throughout the tests.

The potential was scanned during the test by using a Princeton Applied Research potentiostat (Model 173) equipped with an electrometer probe (Model 178), logarithmic current converter (Model 376) and programmer (Model 175). The potential and logarithm of current were recorded on an X-Y recorder.

2.1.2 Procedure

The test solution was placed in the cell, then brought

to the test temperature. The specimen was inserted and a cathodic potential (< 1.25 V_{SCE}) was applied for 30 minutes to remove any oxide films. Afterwards, the potential was scanned in the anodic direction at 1 mV/sec. Current and potential were recorded automatically.

2.2 Slow Strain Rate Tests

2.2.0 Introduction

Stress corrosion tests were conducted at known potential with respect to the anodic polarization curves in order to correlate SCC with electrochemical behavior.

The slow strain rate test (SSRT) provides a quick test to determine susceptibility to SCC.[11,63] A waisted, cylindrical tensile specimen, surrounded by test solution, is pulled at a very slow rate until it fails. Potential is controlled during the test.

If the test is conducted under inert conditions, the failure is ductile, and the specimen necks before fracture so that the final area of the fractured surface is small. If the test is conducted under conditions of susceptibility, cracking occurs. The test is shorter because the specimen fractures before it has necked partly or fully and the final area of the fracture is larger. By measuring the areas of the fractures

as a fraction of the original cross-sectional area of the specimen, susceptibility can be determined. If susceptible, the percent reduction in area will be less than it would be in inert conditions. The percent reduction in area is plotted versus potential to determine regimes of SCC susceptibility.

2.2.1 Materials and Preparation

Type 316 stainless steel, received as 9.5 mm diameter rod, was used to fabricate the SSRT specimens. The material composition has been listed in Table I. The specimens were 25.4 cm long, threaded at each end. A central 25.4 mm cylindrical gage section 4 mm in diameter was machined in each specimen.

Most specimens were tested as received. One was tested after being annealed at 1050 °C for 1 hour, then quenched in water. Three were tested after being annealed for 1 hour, sensitized at 650 °C for 2 hours, and then quenched in water. Sensitization treatment was similar to that used by others.[10,64] During heat treating the specimens were enclosed in stainless steel (Sen Pak) envelopes. The mechanical properties for the 3 material histories are listed in Table II.

The specimen gage sections were polished with 3/0 emery paper and degreased with chlorethane. Each specimen was wrapped with Teflon tape, leaving only the gage section exposed.

Table II Mechanical Properties of SSRT Specimens

Material History	Yield Strength at 92 °C MPa	Ultimate Tensile Strength at 92 °C MPa	Hardness HRB
As-received	283	530	87
Annealed	170	-	72
Annealed & Sensitized	170	-	70

The specimens were stored in a desiccator until needed.

The cell used for the SSRT is illustrated schematically in Figure 2. Its construction was similar to that of the cell used in the polarization studies. The specimen fitted tightly into the cell bottom to prevent leakage of the solution. The threaded ends of the specimen screwed into grips which pinned into a floor model Instron testing machine. Heating tape, wrapped around the cell, was regulated with a thermistor probe and temperature controller as described in Section 2.1.1.

The potential was measured with respect to a room temperature saturated calomel reference electrode (SCE) and controlled to $\pm$ 0.005 V during the test with the same potentiostat used in the polarization studies. A roll type chart was used to record load versus elongation during the test. Solutions were made as described in Section 2.1.1.

2.2.2 Procedure

The SSRT specimen was inserted in the test cell and placed in the Instron. The solution for the test, freshly mixed and heated to temperature was poured into the cell. Nitrogen purge was begun immediately to provide stirring and to prevent oxidation of sulfide in those tests using sulfide. Heating tape was wrapped around the cell and heat applied.

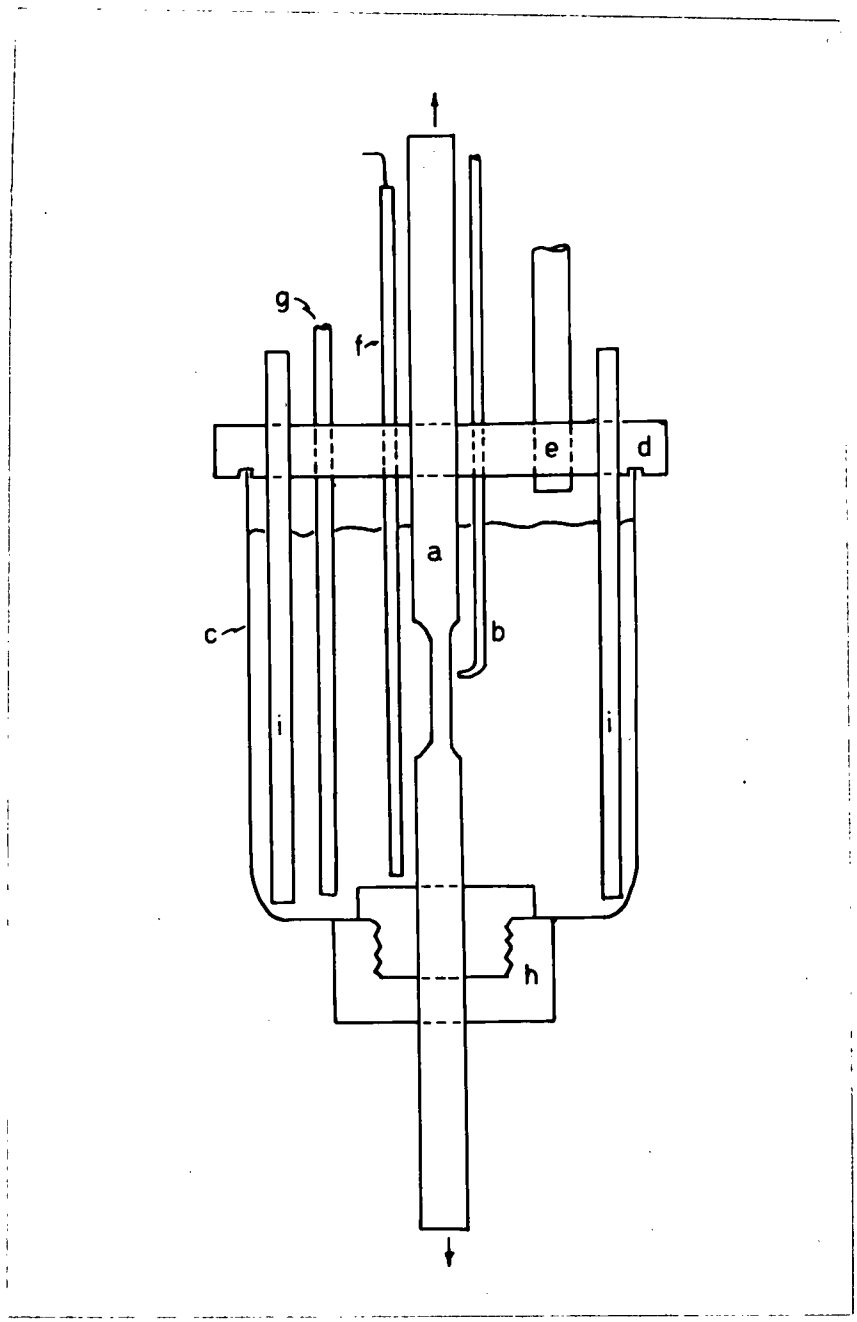

Figure 2 Slow strain rate test cell
a) specimen b) Luggin capillary c) cell
d) lid e) reflux condenser f) temperature
probe g) nitrogen purge h) Teflon cell
bottom i) counter electrode

A cathodic potential of -1.25 V_{SCE} was applied to the specimen for 30 minutes prior to the test to reduce any surface film. The potential was then set to the test potential. After another 30 minutes, the crosshead of the Instron was set in motion to give a strain rate of $3.3 \times 10^{-6} S^{-1}$ and the load recorded.

Each test lasted $\sim$ 48 hours, ending with fracture. If SCC occurred, the test time was shorter. When the specimen was removed from the cell, the diameter of the fracture surfaces was measured with a travelling microscope and the percent reduction in area calculated.

The fracture surfaces of the specimens were examined and photographed in a scanning electron microscope. In some of the tests, one-half of the failed gage section was mounted in 'Quickmount' epoxy and polished to 1 μm with diamond paste. The mounted specimen was then etched with a mixture of 10 ml HNO_3, 10 ml CH_3COOH, and 18 ml HCl with 4 drops of glycerol. Examination and photography were conducted with a Zeiss Ultraphot optical microscope.

An aliquot of solution was taken from one test to determine chloride concentration resulting from leakage of KCl from the Luggin capillary. An automatic titrator (Radiometer TTT80) and an automatic burette (Radiometer ABU-80)

were employed in the analysis.

2.3 Fracture Mechanics Testing

2.3.0 Introduction

Polarization studies and slow strain rate tests together provide information on the potential at which SCC may occur in a given environment, and on the electrochemical reactions promoting susceptibility. Fracture mechanics testing can add to this understanding by giving information on kinetic factors and providing useful information for equipment designers and operators.

Specimens used in fracture mechanics testing are pre-notched and fatigue pre-cracked to overcome initiation problems and provide data on crack growth kinetics. The specimens are designed so that load, crack length, and stress intensity may be related by a known K_I-calibration relation. The stress intensity, K_I, can then be calculated for a given load and crack length to give a measure of the intensity of stress at the crack tip.[48,65] Rate of crack growth may be related to stress intensity throughout the test. In corrosive environments, there is often a stress intensity below which no cracking can be detected; this is called K_{ISCC}.[65] As K_I is raised above this value, crack growth rate rises too. This region of K_I-dependent velocity is called Region I. A region of K_I-independent crack growth rate extends through

intermediate values of K_I; this is Region II. Finally the growth rate begins to increase again until failure occurs at K_{IC}; this is Region III. This behavior has been observed by a number of investigators for a variety of alloys and solutions.[13,48,49]

K_{ISCC} is difficult to determine because cracking rate becomes infinitely slow as K_I is decreased toward K_{ISCC}. Initiation would have to take place just above K_{ISCC} because the K_I value increases during cracking for this specimen design.

Region I is of interest to designers because equipment which is cracking spends a large portion of its life there. Region II is also important and it is of special interest to researchers studying the causes of SCC because the crack growth kinetics in that region are controlled solely by stress independent processes.

The T-notch double cantilever beam (TN-DCB) was originated by Russel and Tromans.[14] It is illustrated in Figure 3.

The K_I calibration for the TN-DCB specimen is given by:

$$K_I = (1.172 \times 10^5)\, P(a)^{0.5} [2.43 - 3.62(a/0.032) + 14.5(a/0.032)^2 - 24.6(a/0.032)^3 + 26.5(a/0.032)^4] \quad \ldots(1)$$

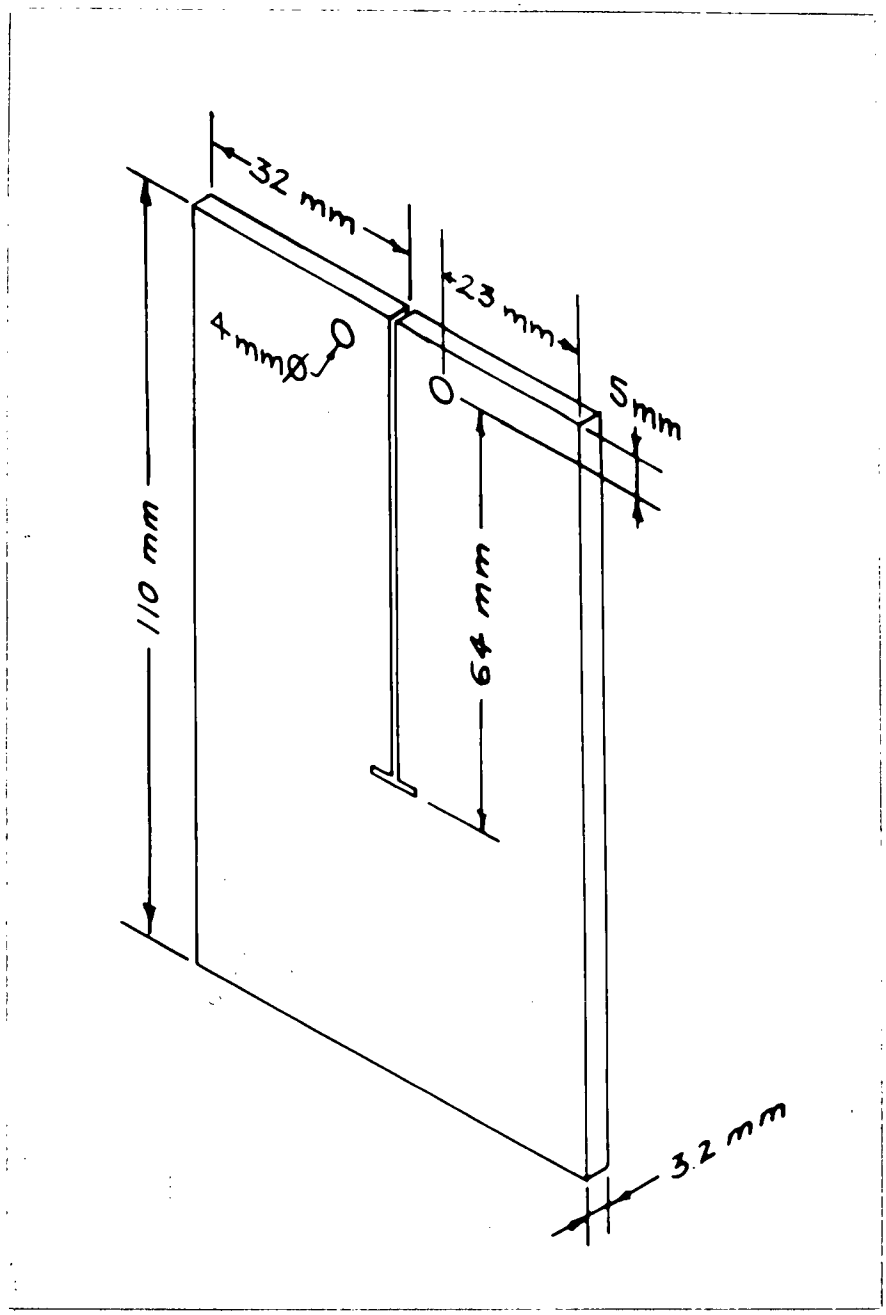

Figure 3 T-notch double cantilever beam specimen.

Errors due to the downward growth of cracks have been calculated by Russel,[48] but have been considered to be negligible in this present study.

The TN-DCB has been used here because:

1. It is thin, so the crack length measured in the surface will not differ greatly from the crack front at the center.

2. Research has been done on this material in $MgCl_2$ using this specimen design.[14,48] This similarity will aid comparison of behavior in these different environments.

The specimen has some disadvantages:

1. The very low loads required to produce a fatigue pre-crack are difficult to apply accurately and the stress intensities required to pre-crack preclude SCC testing below that stress intensity.

2. The specimen is thin, so plane strain conditions would not be satisfied at high stress intensities, depending on yield strength.

To fulfil the criterion for plane-strain testing the specimen thickness must be $\geq 2.5\ (K/\sigma_y)^2$.[66] For the material used, plane strain conditions are satisfied only to a stress

intensity value of 17 MPa$\sqrt{m}$ (assuming σ_y = 475 MPa). In spite of this, testing was conducted up to 100 MPa$\sqrt{m}$ at which point gross deformation began. The cracks were straight and did not seem to avoid propagation through plane-stress plastic zones as has been suggested.[67]

2.3.1 Materials and Preparation

Type 316 stainless steel from a single plate was used. Its composition has been listed in Table I.

The plate was cold-rolled to an intermediate thickness, then annealed at 1050 °C for 30 minutes in a stainless steel foil envelope (Sen Pak). It was then quenched in water. Further cold rolling left the material with a thickness of 3.2 mm and 25% cold work. The cold worked plate had a yield strength of 475 MPa and ultimate tensile strength of 830 MPa. Hardness measured HRC 25. The plate material and worked condition were identical to those employed by Russel.[14,48]

One specimen was made of material which was rolled to its final thickness then annealed at 1050 °C for 1 hour. Thus, it was free of cold work. Hardness measured HRB 76.

Specimens were machined from the rolled material so that cracks would propagate in the rolling direction. The specimens were polished to 600 grit on one side and the surface

was scribed with fiducial lines 1 mm apart to be used to measure crack velocity.

Starter cracks were sawn in each specimen with a jewellers saw. The specimens were fatigue pre-cracked to reduce initiation time. The fatiguing was carried out at a maximum stress intensity value lower than that to be used in the test. A Sonntag fatigue machine was utilized for pre-cracking.

Finally the specimens were wrapped with Teflon tape leaving a band of exposed area in the vicinity of the crack and its region of propagation.

The corrosion cells used in the tests were of a similar construction to that used in the polarization studies (Section 2.1.1). The solutions were mixed in the same way, nitrogen purging continued throughout the tests, temperature was controlled to $\pm$ 1 °C, and potential was controlled to $\pm$ 0.005 V with respect to an external standard calomel electrode.

Each specimen was mounted in its test cell and loaded as shown in Figure 4. Tensometers (Hounsfield and Monsanto) were used mostly, with a spring in series with the specimen to minimize load drop resulting from cracking. Some specimens were loaded by a calibrated homemade device which used a

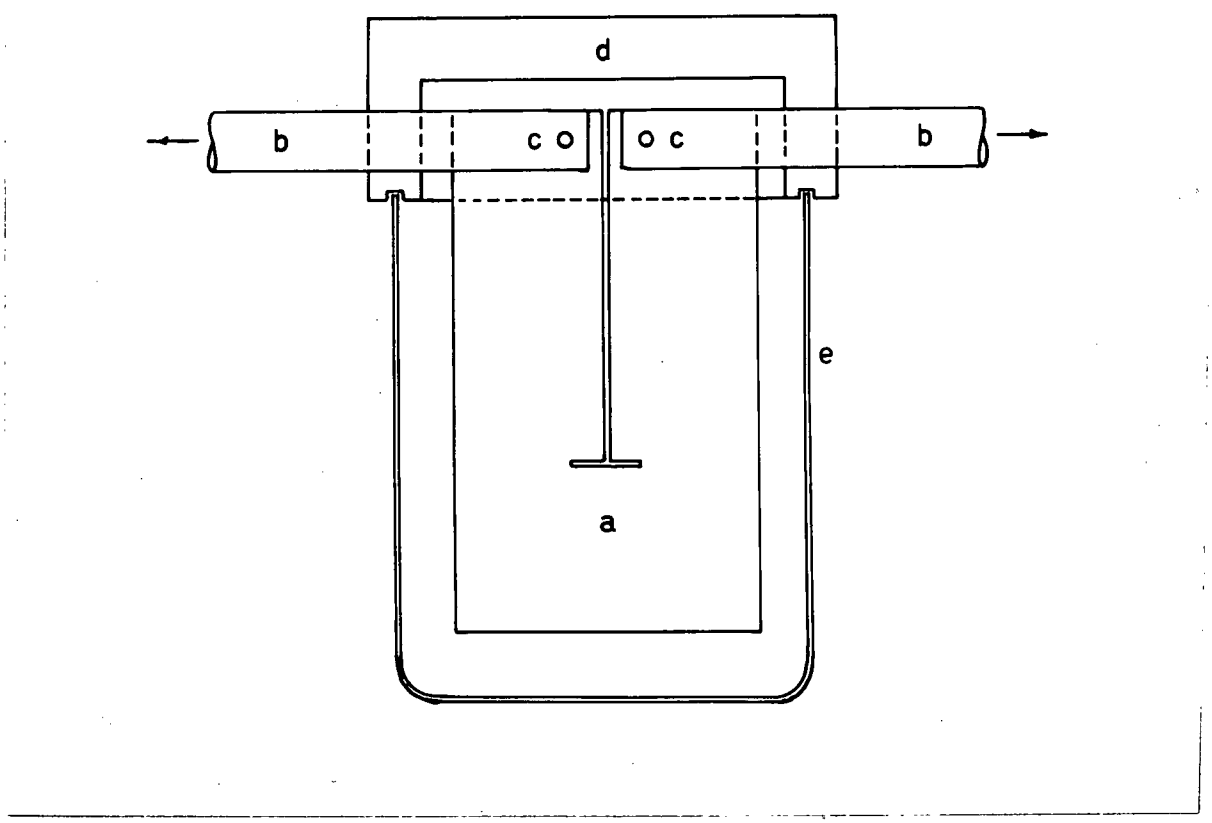

Figure 4 Fracture mechanics testing cell

a) specimen b) grips

c) pins d) cell lid

e) beaker.

weighted lever to apply the load.

The potential was applied in the same manner as for the slow strain rate tests. A variety of potentiostats was used, including ECO model 549 and Wenking models OPA 69 and 68TS10.

2.3.2 Procedure

The specimen and cell were placed in the tensometer, the solution was added, and potential was applied. No cathodic potential was applied to reduce surface films prior to the test. Load was applied 30 minutes after establishing the potential control. The Luggin capillary had to be replaced about once per week because the cotton thread dissolved out of its tip and a bubble formed, breaking the circuit.. The test solution was replaced periodically with fresh solution. The level of solution in the cell was maintained daily by adding a few milliliters of boiled distilled water.

The cell was opened every few days to measure the crack length. This was done visually with the aid of the scale scribed on the specimen surface. Time, load, crack length and calculated stress intensity were recorded. In those cases where cracking occurred on one side of the specimen only, the other side was sawed periodically to a matching length to maintain proper loading geometry.

At the completion of some of the tests, the corrosion cell was lowered away from the specimen and the surface of the specimen was dried quickly with absorbent paper tissue. pH indicator paper (pHydrion) with pH intervals of 0.5, was pressed against the specimen at the crack, so that the paper absorbed solution draining from the crack. The indicator paper showed that this crack solution has a pH of $\sim$ 14 at room temperature.

The Teflon tape was removed and the specimen was rinsed with distilled water and ethanol before being sectioned. Specimens with heavy corrosion deposits were cleaned ultrasonically with an inhibited acid solution composed of 3 ml HCl, 4 ml 2-Butyne-1,4 diol (35% aqueous solution) plus 50 ml distilled water which produced no artifacts.[68]

The fractography was examined in an ETEC scanning electron microscope at 20 keV.

The crack lengths measured during the test were plotted versus time. A line was fitted to this data using the least squares method if three approximately colinear points were available. Otherwise the line through two points was calculated. This was the case for most Region I data. Differentiation of the equation for the line yielded the velocity. The

velocity has been plotted as a constant value for Region II (stress intensity independent cracking). Error was calculated for 95% confidence limits using constants from Student's t-distribution as described by Stanton.[69] Values for apparent activation energy were calculated in the same manner using 90% confidence limits.

2.4 Electron Diffraction Analysis of Surface Films

2.4.0 Introduction

Analysis of the corrosion films remaining on the fracture surfaces[70] may provide important clues about the mechanism of cracking. Differences in composition between the film and the matrix may show which elements have been dissolved during cracking. The film structure may be formed of the products of various dissolution reactions. Examination of the crystal structure may provide insight into these reactions.

2.4.1 Sampling for Corrosion Film Analysis

Fracture mechanics (TN-DCB) specimens from tests in 3.35 mol/kg NaOH at 92 °C were sectioned with a jewellers saw to expose the fracture surfaces. Sections were placed in shallow dishes and submerged in a solution of 1 volume percent bromine in methanol as described by Nikiforuk.[70] After 2 days, the sections were tapped lightly to dislodge

the film and then removed. Small pieces of the surface film were left floating in the methanol-bromine mixture. These were picked up with a fine copper electron microscope specimen grid and placed in methanol to remove traces of bromine. Subsequently, the films were picked up with a fine copper grid covered with a support film of carbon and placed on absorbent filter paper to dry. Afterwards the grid with films was stored in a desiccator.

2.4.2 Procedure

The grating with film on it, was inserted in a sample holder and placed in the transmission electron microscope, Hitachi model HU-11A, for examination at 100 keV. A field limiting aperture was used to select the area from which an electron diffraction ring pattern would be obtained.

After the photographic plate was exposed to the electron diffraction pattern, the diffraction ring pattern of an evaporated gold film standard was photographed. This served as a calibration standard.

The distances, d, between crystal planes in the lattice were known for the gold standard. The diameter, D, of the corresponding diffraction rings were measured on the diffraction pattern. Using equation 2, it was possible to

determine the camera constant, κ

$$Dd = \kappa \qquad \ldots(2)$$

The diameters of the rings were measured on the diffraction pattern of the unidentified surface film, and using the camera constant, the d-spacing was calculated. The d-spacing and the relative intensities were matched with those listed in the powder diffraction catalog[71] to identify the compound in the film. These were confirmed by comparison with theoretical estimates of relative intensities for electron diffraction in Fe_3O_4 as calculated by Birley.[72] The patterns were found to be characteristic of spinel structures exhibiting cubic symmetry for which:

$$d_{hkl} = a_o/(h^2+k^2+l^2)^{0.5} \qquad \ldots(3)$$

where a_o is the lattice parameter and h, k and l are the Miller indices of the plane of interest.

The factor $\sqrt{h^2+k^2+l^2}$ was plotted versus the diameter of the rings of the diffraction pattern and a line was fitted to the data. From this, the lattice parameter, a_o, could be calculated using equation 3.

3. RESULTS

3.1 Anodic Polarization Curves

3.1.0 NaOH

The anodic polarization curves have been drawn with respect to two different potential scales: the standard calomel electrode, V_{SCE}, and the standard hydrogen electrode, V_{SHE}. These are related by:

$$V^{\circ}_{SHE} = -0.2416\ V_{SCE} \qquad ...(4)$$

No correction was made to the potential to account for thermal gradient effects and liquid junctions.

Figure 5 shows the curve for 316 stainless steel rod in 3.35 mol/kg NaOH at 92 °C. The active-passive transition "nose" located at -1.00 V_{SCE} was flat and double peaked. The primary passive range extended from -0.75 to -0.25 V_{SCE} and a primary transpassive region was observed at -0.10 V_{SCE}. From 0 to 0.25 V_{SCE} there was a secondary passive region.

Figure 6 shows the polarization curve for the plate material. It was similar to Figure 5 except that the active-passive "nose" exhibited a single peak.

The effect of NaOH is shown in Figure 7. Increasing the concentration increased the current density, and displaced

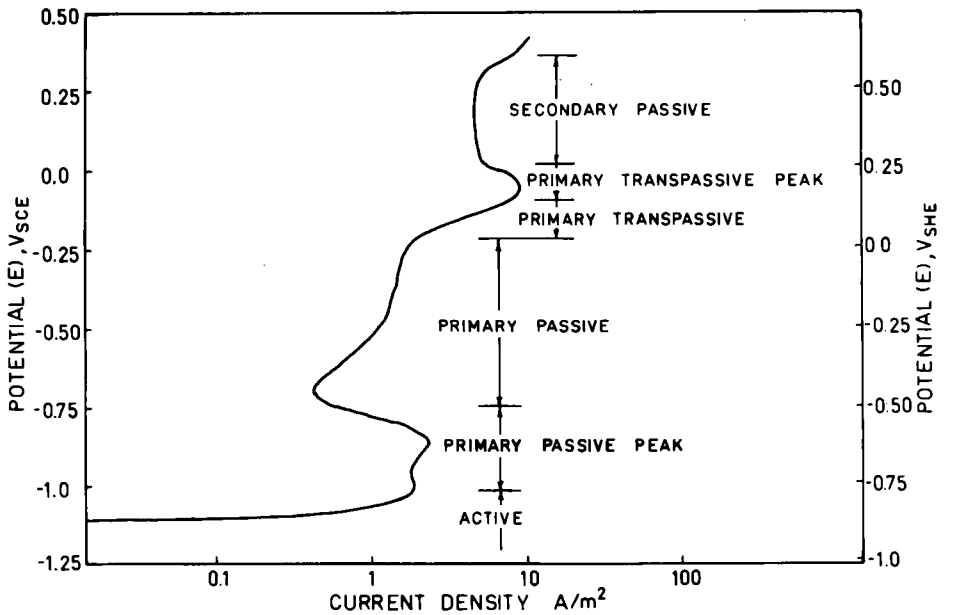

Figure 5 Anodic polarization curve, 316 stainless steel rod, 3.35 mol/kg NaOH, 92 °C.

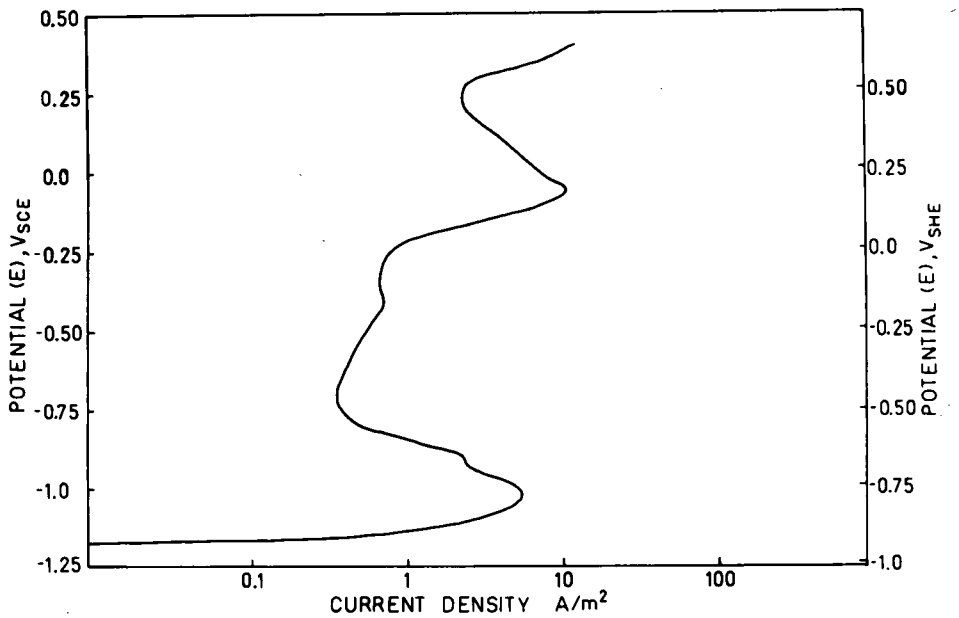

Figure 6 Anodic polarization curve, 316 stainless steel plate, 3.35 mol/kg NaOH, 92 °C.

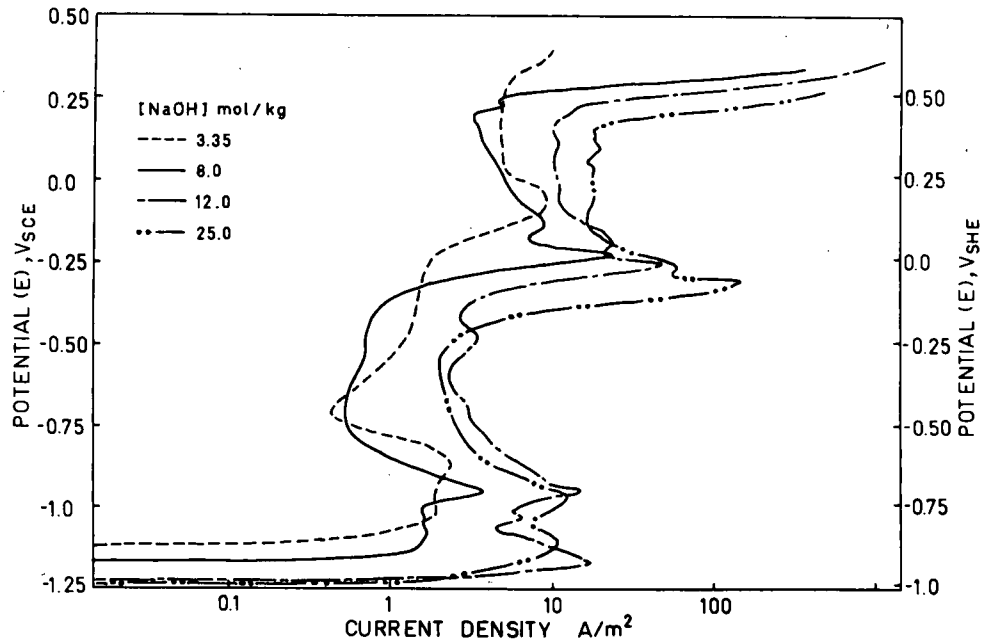

Figure 7 Anodic polarization curves at selected NaOH concentrations, 316 stainless steel rod, 92 °C.

the primary transpassive peak and corrosion potential to lower (more active) values.

Raising the temperature increased the current density in 3.35 mol/kg NaOH and lowered the potential of the transpassive peak as illustrated in Figure 8.

Figure 9 illustrates the polarization curves for chromium in two concentrations of NaOH. The transpassive current density was shifted to lower potential in the more concentrated solution. The corrosion potential, E_{CORR}, was in the passive region in 3.35 mol/kg NaOH and in the active region in 8 mol/kg NaOH, accounting for the active-passive transition at -1.10 V_{SCE} in the latter. The solution was yellow after completion of the anodic scan.

The polarization behavior of nickel is shown in Figure 10. There was an active-passive peak at -0.85 V_{SCE} and a passive region at more noble potentials.

Iron had an active-passive current peak at -1.05 V_{SCE} as shown in Figure 11.

3.1.1 NaOH + Na_2S

Figure 12 shows the polarization curve for the 316 stainless steel rod in 2.5 mol/kg NaOH + 0.423 mol/kg Na_2S

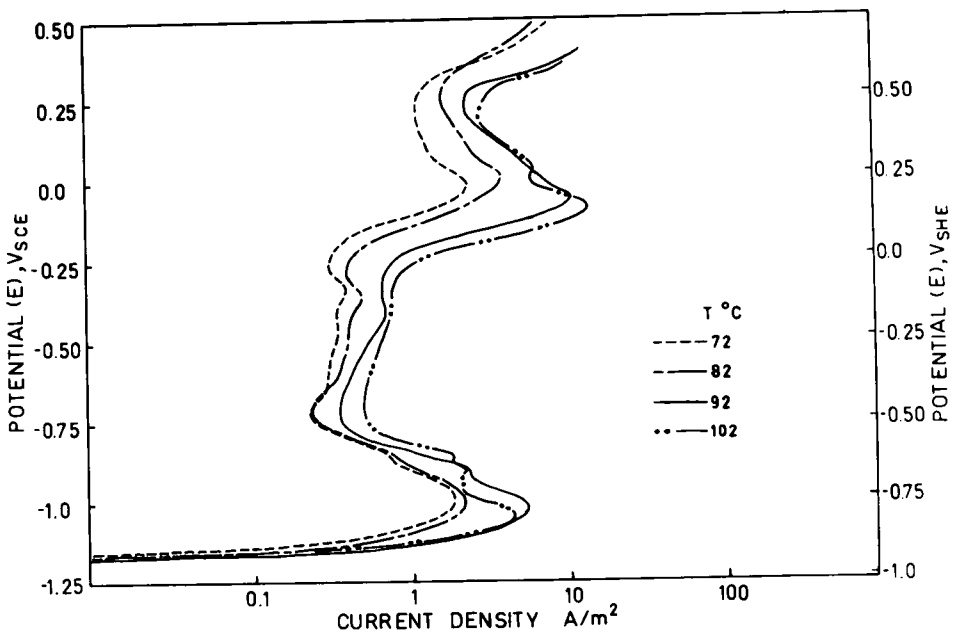

Figure 8 Anodic polarization curves at selected temperatures, 316 stainless steel rod, 3.35 mol/kg NaOH.

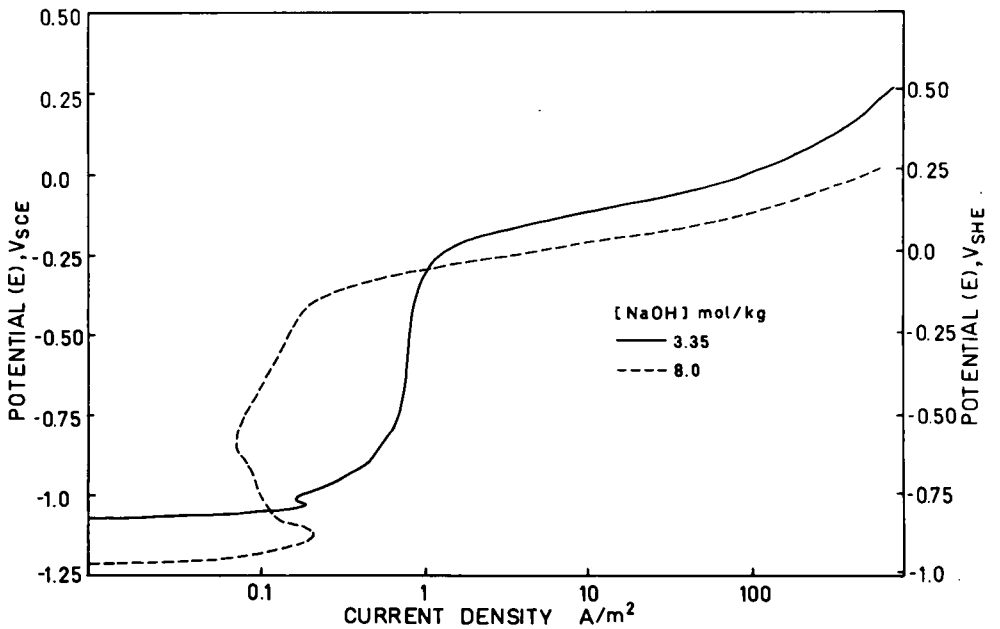

Figure 9 Anodic polarization curves, chromium, 3.35 and 8 mol/kg NaOH, 92 °C.

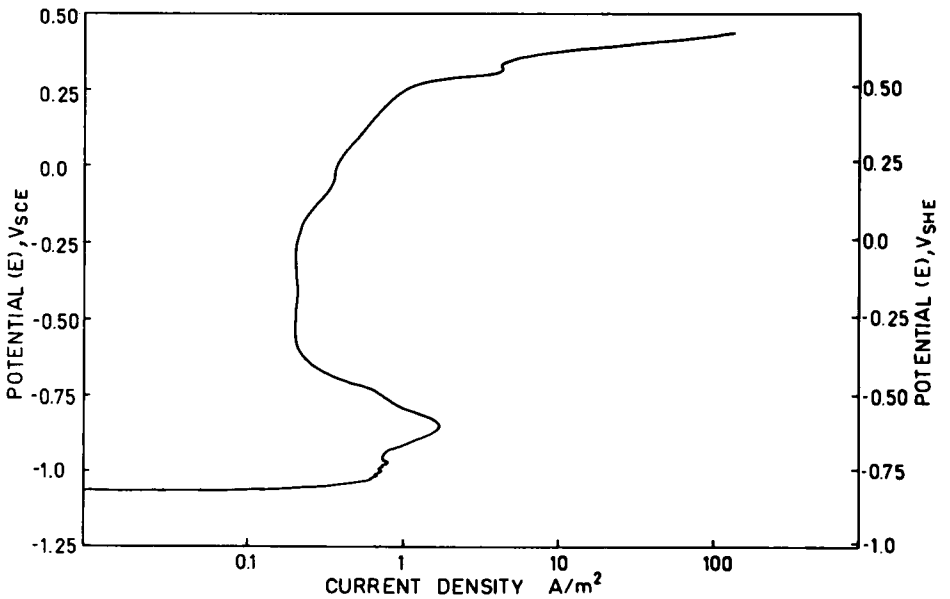

Figure 10 Anodic polarization curve, nickel, 3.35 mol/kg NaOH, 92 °C.

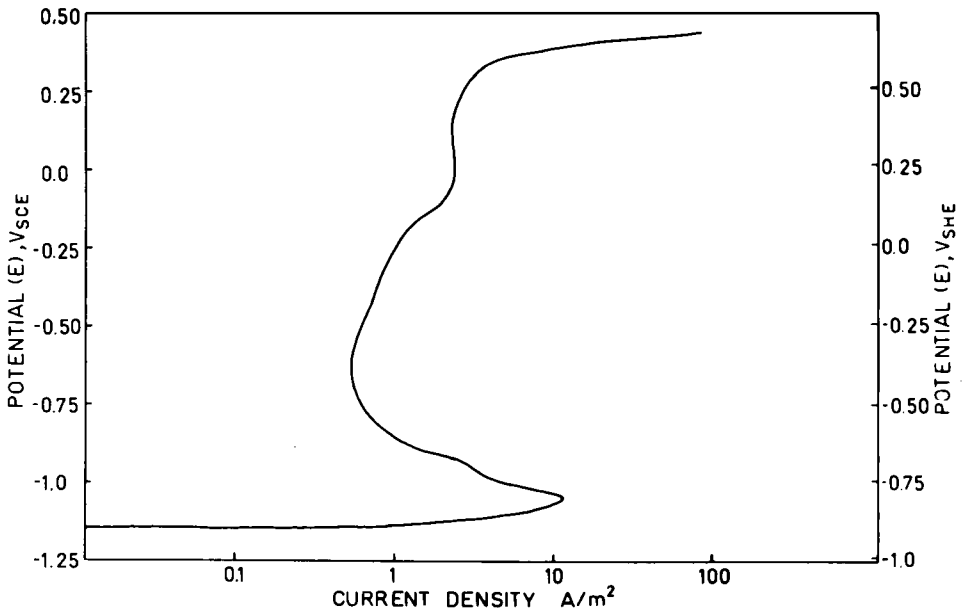

Figure 11 Anodic polarization curve, iron, 3.35 mol/kg NaOH, 92 °C.

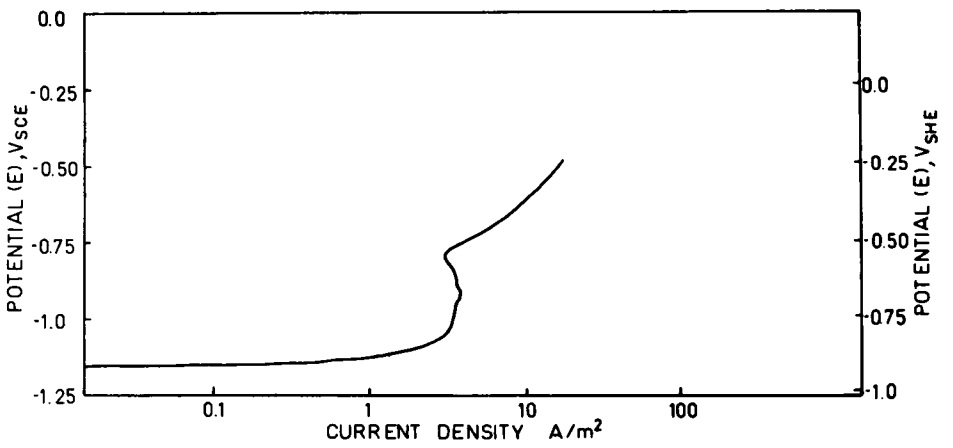

Figure 12 Anodic polarization curve, 316 stainless steel rod, 2.5 mol/kg NaOH + 0.423 mol/kg Na_2S, 92 °C.

at 92 °C. The current density between -1.15 and -0.75 V_{SCE} was of the same order of magnitude as that of the active-passive current peak in the solution without sulfide.

Figure 13 illustrates the effect of increasing concentrations of NaOH. The corrosion potential, E_{CORR}, was in the active region and an active-passive transition was evident. The current peak became larger as the NaOH concentration was increased, and was much larger than that in the sulfide free solutions.

The effect of temperature in 2.5 mol/kg NaOH + 0.423 mol/kg Na_2S is illustrated in Figure 14 for plate material. The current density increased and E_{CORR} decreased as the temperature was increased. Two small current peaks were observed at the active-passive transition, similar to those seen in the NaOH solutions. The current peaks were insignificant compared to those shown in Figure 13.

3.2 Slow Strain Rate Tests

3.2.0 NaOH

The percent reductions in cross-sectional area of the SSRT specimens are plotted versus potential in Figure 15. The minimum reduction in area occurred at -0.50 to -1.50 V_{SCE}. This indicated that the greatest susceptibility to SCC

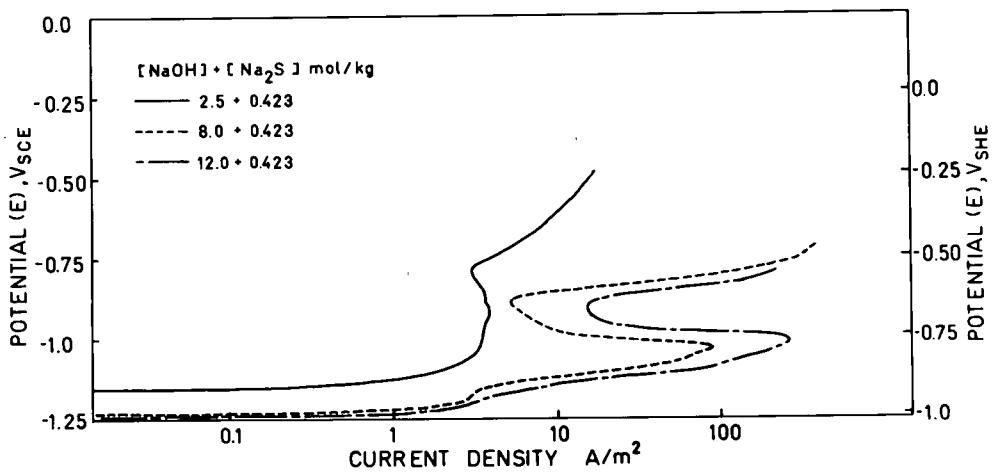

Figure 13 Anodic polarization curves in solutions of selected NaOH concentration with Na_2S, 316 stainless steel rod, 92 °C.

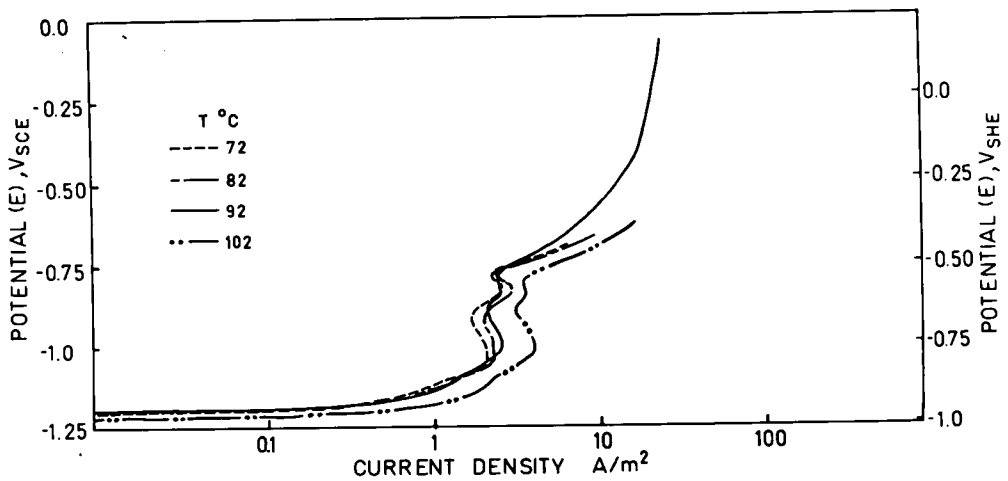

Figure 14 Anodic polarization curves at selected termperatures, 316 stainless steel plate, 2.5 mol/kg NaOH + 0.423 mol/kg Na_2S.

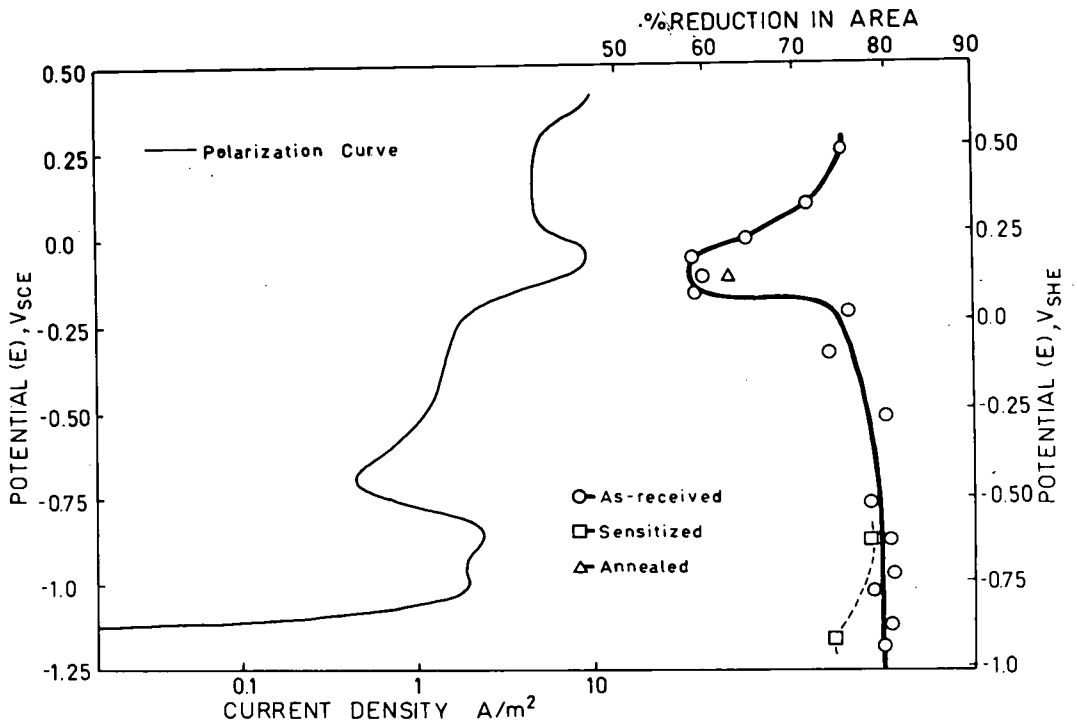

Figure 15 Effect of potential on percent reduction in area during slow strain rate tests, 3.35 mol/kg NaOH, 92 °C. Anodic polarization curve for 316 stainless steel rod.

was near the primary transpassive peak.

Figure 16 shows the appearance of the fracture region of the specimen tested at -0.10 V_{SCE}. The surface was severely attacked and exhibited intergranular cracks. The surfaces of specimens tested at 0.10, 0, -0.50 and -0.15 V_{SCE} were cracked similarly. The fracture sections indicated that cracking occurred in the secondary passive region but not in the primary passive region. Surface cracking was absent at lower potentials near the active-passive transition, as shown at -0.95 V_{SCE} in Figure 17.

An annealed specimen tested at -0.10 V_{SCE} showed slightly less susceptibility to SCC than the as-received material.

A sensitized specimen tested at -1.15 V_{SCE} was slightly more susceptible. One tested at -0.85 V_{SCE} showed no difference from the as-received material.

The surface film observed on the specimens varied with the potential. It was dark red-brown above about -0.50 V_{SCE}. At 0.25 V_{SCE}, it appeared to be thick and fairly brittle, as seen in Figure 18a. At -1.0 V_{SCE}, the surface film appeared to be very much thinner with a distorted appearance as shown in Figure 18b.

Figure 16 SSRT specimen after testing at -0.10 V_{SCE} in NaOH solution.

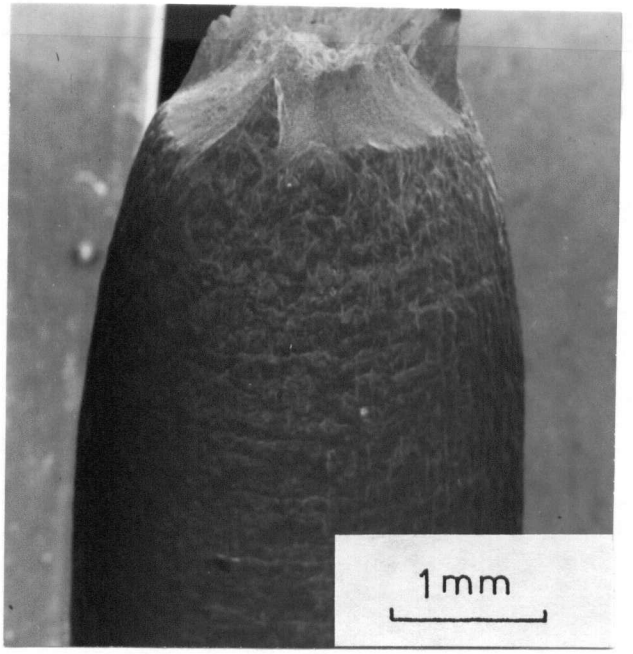

Figure 17 SSRT specimen after testing at -0.95 V_{SCE} in NaOH solution.

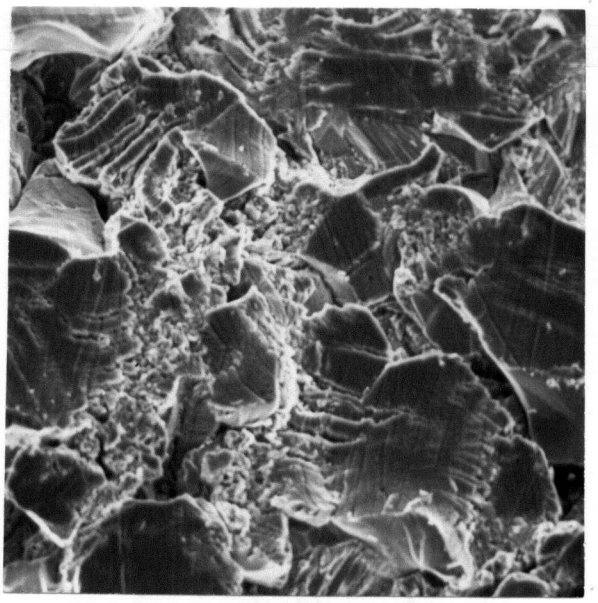

a

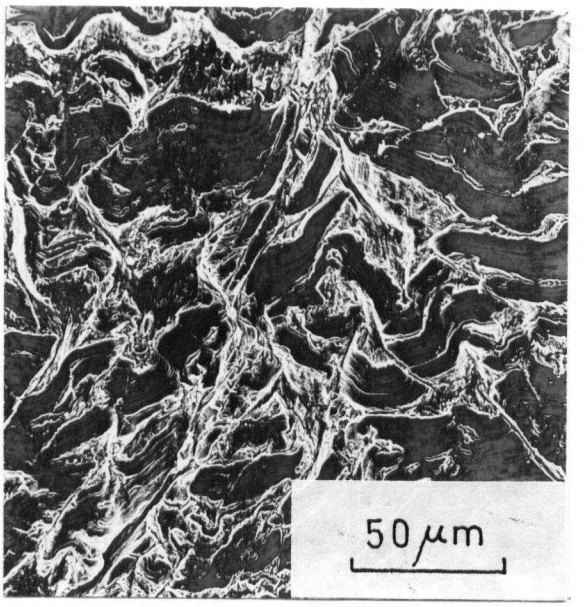

b

Figure 18 Surface film on SSRT specimens tested in NaOH solution a) 0.25 V_{SCE}, b) -1.00 V_{SCE}.

The solution from one test (-0.25 V_{SCE}) was analyzed for $[Cl^-]$. The concentration was ~ 0.03 mol/kg after a 2 day test.

3.2.1 NaOH + Na_2S

The percent reductions in cross-sectional area of the SSRT specimens are illustrated in Figure 19. Some susceptibility to SCC in the active region was indicated by the decrease in reduction in area at -1.15 V_{SCE}. Tests were not conducted at higher potentials due to oxidation of sulfide ions as evidenced by the increase in current above -0.75 V_{SCE}.

The fractured region of the specimen tested at -1.15 V_{SCE} is illustrated in Figure 20. There were no cracks in the surface film between -0.85 and -0.95 V_{SCE}.

No effect of sensitization was observed in specimens tested at -1.00 and -1.15 V_{SCE}.

3.3. Fracture Mechanics Testing

3.3.0 NaOH

3.3.0.0 Effect of Stress Intensity

Figure 21 is a plot of crack growth rate versus K_I in 3.35 mol/kg NaOH, 92 °C, -0.10 V_{SCE}. The data show Region I

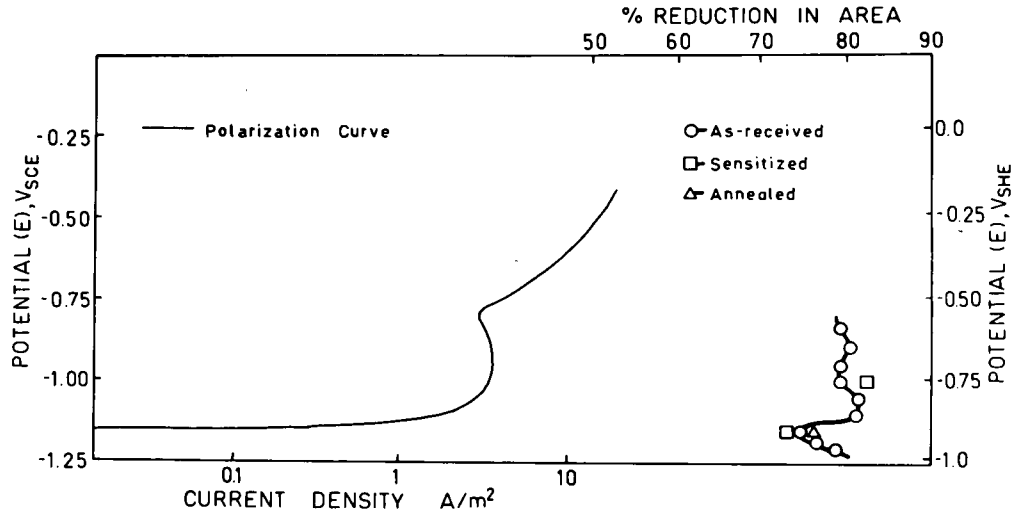

Figure 19 Effect of potential on percent reduction in area during slow strain rate tests, 2.5 mol/kg NaOH + 0.423 mol/kg Na_2S, 92 °C. Anodic polarization curve for 316 stainless steel rod.

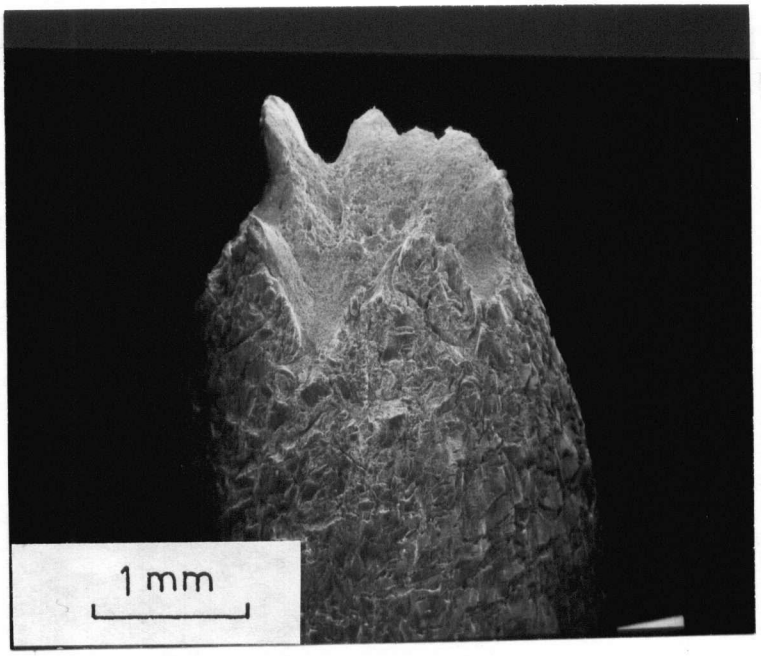

Figure 20 SSRT specimen after testing at -1.15 V_{SCE} in NaOH + Na_2S solution.

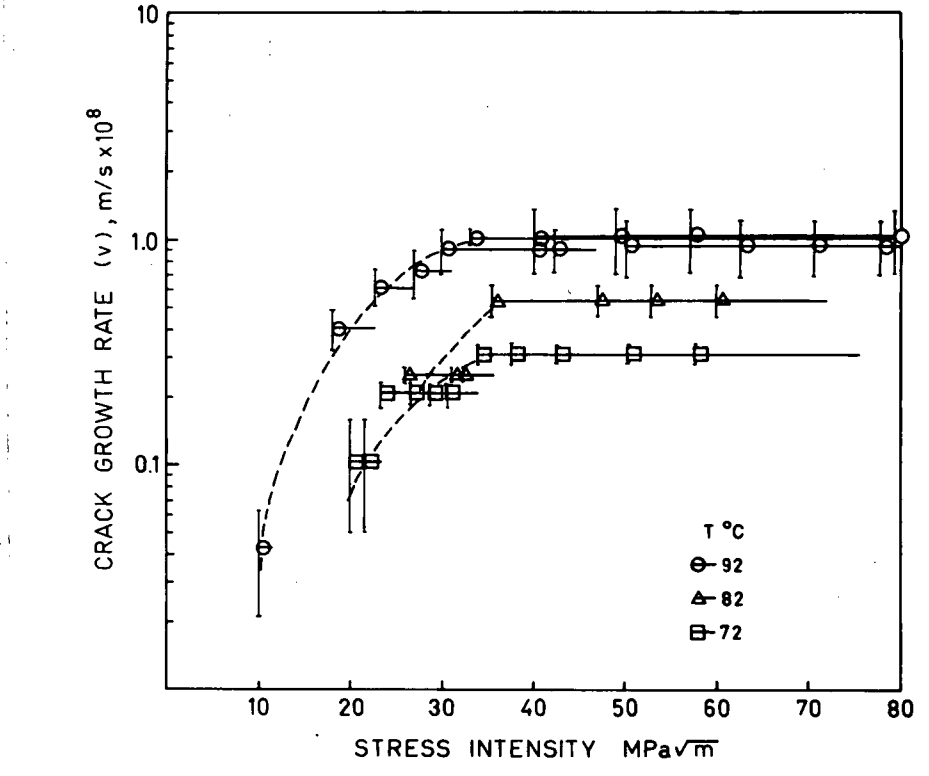

Figure 21 Crack growth rate versus stress intensity at selected temperatures in 3.35 mol/kg NaOH, -0.10 V_{SCE}.

(K_I dependent) and Region II (K_I independent) behavior. Region I data were difficult to obtain because cracking was so slow. K_{ISCC} appeared to be less than 10 MPa$\sqrt{m}$. The data used to construct Figure 21 are summarized in Table III.

3.3.0.1 Temperature Effect

Crack growth rate data in 3.35 mol/kg NaOH at 92, 82 and 72 °C are listed in Table III and illustrated in Figure 21. Results obtained in 12 mol/kg NaOH at 92 and 82 °C are also listed in Table III and are shown in Figure 22. The potential was maintained at -0.10 V_{SCE} in all these tests. Crack growth rate decreased with decreasing temperature.

The effect of the temperature on Region II crack growth rate was evaluated assuming a simple Arrhenius rate law:

$$V = V_o \exp(-Q/RT) \qquad ...(5)$$

where

V = crack growth rate

V_o = experimental constant

Q = apparent activation energy

R = gas constant

T = temperature (°K)

The logarithm of crack growth rate was plotted versus 1/T as shown in Figure 23. A line was fitted to the 3.35

TABLE III Summary of Fracture Mechanics Test Data

NaOH Concentration mol/kg	T °C	V_{SCE}	K_I Range MPa$\sqrt{m}$	Crack Growth Rate m/s	Number of Observations
3.35	92	-0.10	10 - 10.6	$(4.29 \pm 2.15)\times10^{-10}$	1
			18 - 22.6	$(4.04 \pm 0.81)\times10^{-9}$	1
			22.6 - 27	$(6.17 \pm 1.23)\times10^{-9}$	1
			27 - 30.7	$(7.26 \pm 1.82)\times10^{-9}$	1
			33 - 52.7	$(1.02 \pm 0.08)\times10^{-8}$	1
			50 - 89.3	$(0.94 \pm 0.27)\times10^{-8}$	8
			40 - 98.3	$(1.02 \pm 0.34)\times10^{-8}$	5
			40 - 110.3	$(1.04 \pm 0.17)\times10^{-8}$	5
			30 - 46.7	$(0.90 \pm 0.18)\times10^{-8}$	7
3.35	82	-0.10	26 - 35.6	$(2.5 \pm 0.19)\times10^{-9}$	6
			35.6 - 72.1	$(5.39 \pm 0.90)\times10^{-9}$	8
3.35	72	-0.10	20 - 23.5	$(1.05 \pm 0.55)\times10^{-9}$	2
			23.5 - 34	$(2.09 \pm 0.22)\times10^{-9}$	4
			34 - 75.4	$(3.09 \pm 0.25)\times10^{-9}$	5
8	92	-0.10	15 - 27.6	$(0.82 \pm 0.16)\times10^{-8}$	3
			27.6 - 73.1	$(1.50 \pm 0.55)\times10^{-8}$	3
12	92	-0.10	16 - 52	$(1.36 \pm 0.16)\times10^{-8}$	8
			15 - 28.8	$(0.99 \pm 0.09)\times10^{-8}$	8
			36.3 - 68.1	$(1.35 \pm 0.11)\times10^{-8}$	5
12	82	-0.10	28.8 - 30.9	$(2.29 \pm 0.02)\times10^{-9}$	5
			30.9 - 94.4	$(0.94 \pm 0.13)\times10^{-8}$	5
3.35	92	0.0	30 - 35.2	$(2.23 \pm 0.29)\times10^{-9}$	6
			35.2 - 64.8	$(3.01 \pm 0.17)\times10^{-9}$	17
3.35	92	-0.175	25 - 46	$(0.31 \pm 0.04)\times10^{-8}$	7

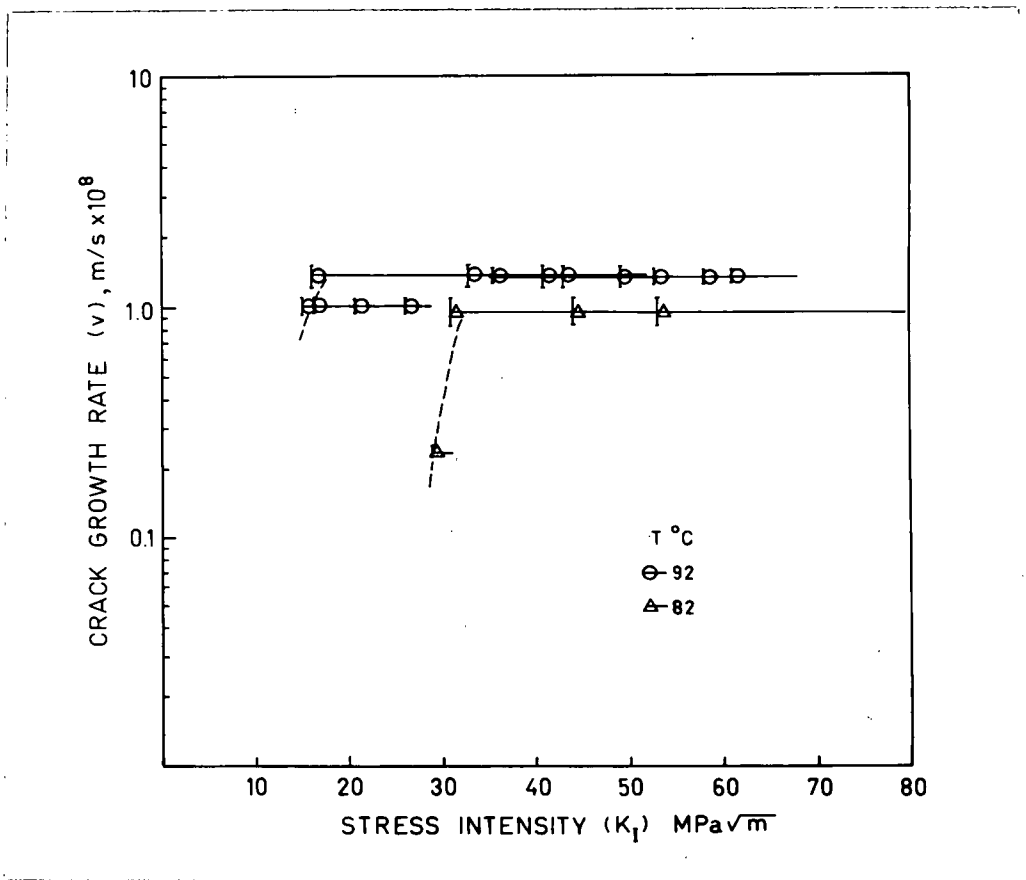

Figure 22 Crack growth rate versus stress intensity at selected temperatures in 12 mol/kg NaOH, -0.10 V_{SCE}.

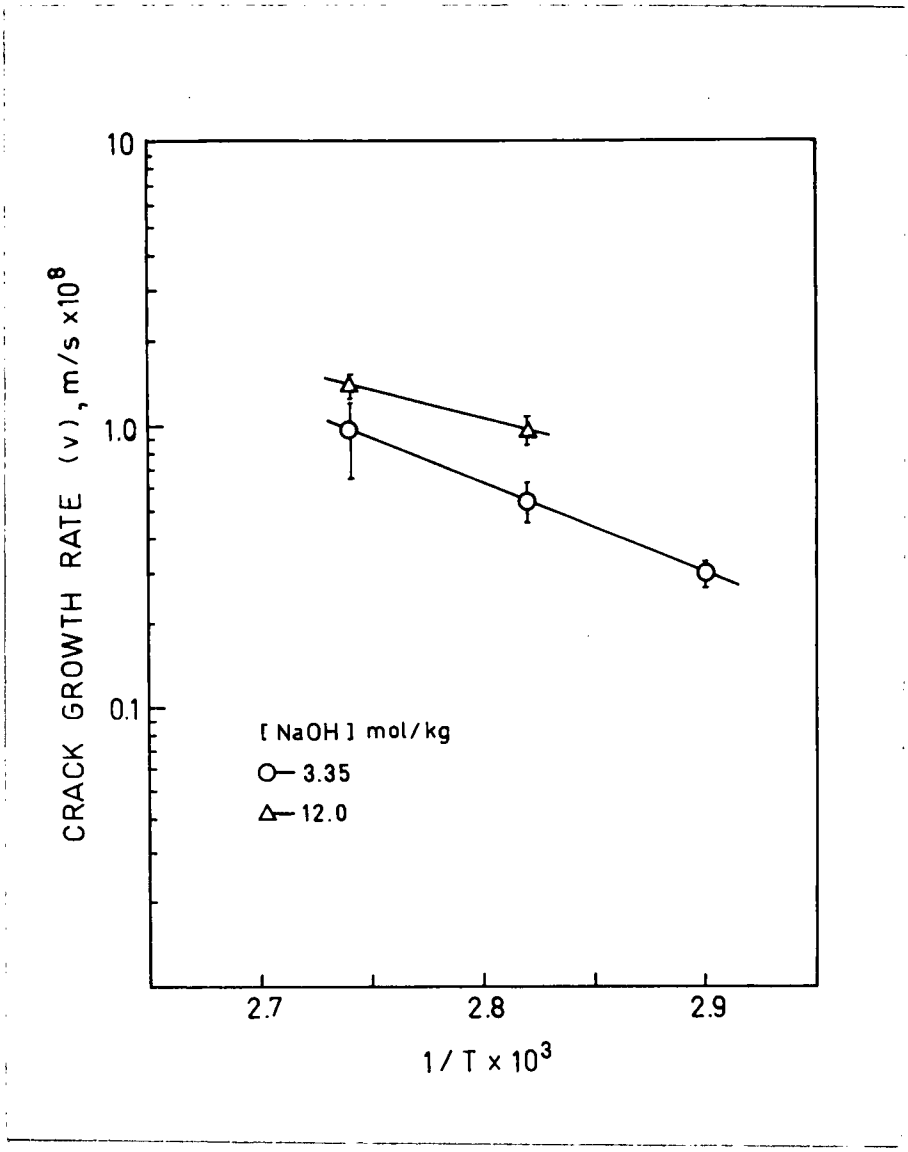

Figure 23 Arrhenius plot of the Region II crack growth rates in 3.35 and 12 mol/kg NaOH, -0.10 V_{SCE}.

mol/kg NaOH data using the least squares method. The apparent activation energy, calculated from the gradient of the line, was 60 $\pm$ 8 kJ/mol (90% confidence). The activation energy in 12 mol/kg NaOH was estimated to be $\sim$ 37 kJ/mol.

3.3.0.2 Effect of NaOH Concentration

The effect of NaOH concentration is illustrated in Figure 24 and tabulated in Table III. The effect of concentration appeared to be small and within the errors of measurement at 8 and 12 mol/kg NaOH. The data of Figure 23 suggests that, although the effect of concentration was small at 92 °C, it had a greater effect at 82 °C.

3.3.0.3 Effect of Applied Potential

Test results obtained at 0, -0.10 and -0.175 V_{SCE} in 3.35 mol/kg NaOH, 92 °C are shown in Table III and Figure 25. The crack growth rate was fastest at -0.10 V_{SCE}, in agreement with the potential of maximum susceptibility in the SSRT.

In addition, fracture mechanics tests were conducted at active-passive potentials. A test conducted in 3.35 mol/kg NaOH at 92 °C, -1.15 V_{SCE} and 30 MPa$\sqrt{m}$, showed no cracking in 10 days. Another test, at -0.85 V_{SCE} and 30 MPa$\sqrt{m}$, showed no cracking after 15 days. Crack growth rates would have been $< 2.89 \times 10^{-10}$ m/s and $< 1.92 \times 10^{-10}$ m/s respectively to be indetectable in the test period.

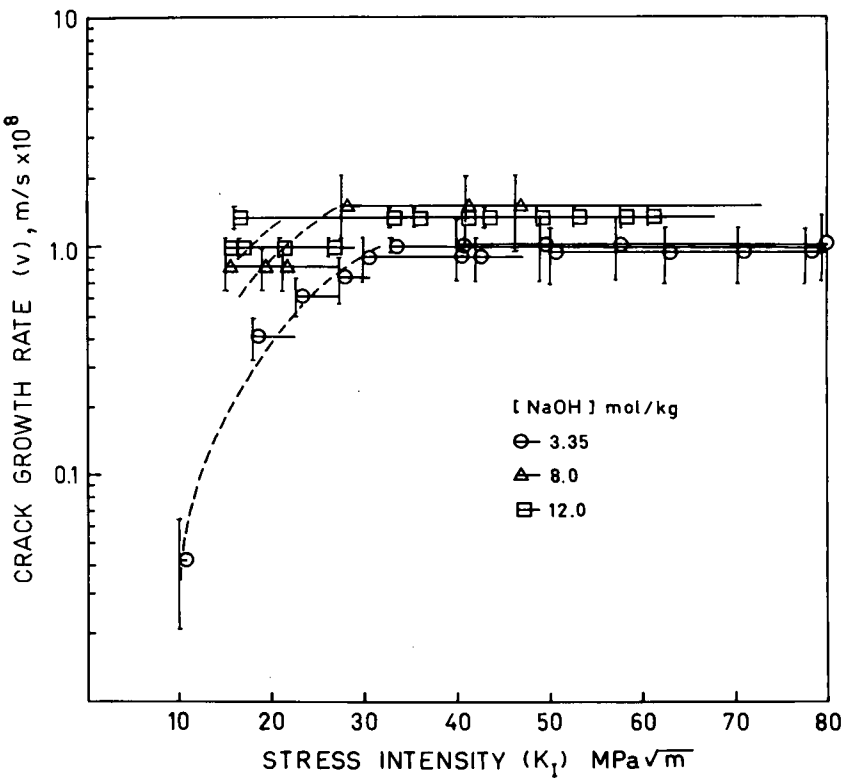

Figure 24 Crack growth rate versus stress intensity at selected NaOH concentrations, 92 °C, -0.10 V_{SCE}:

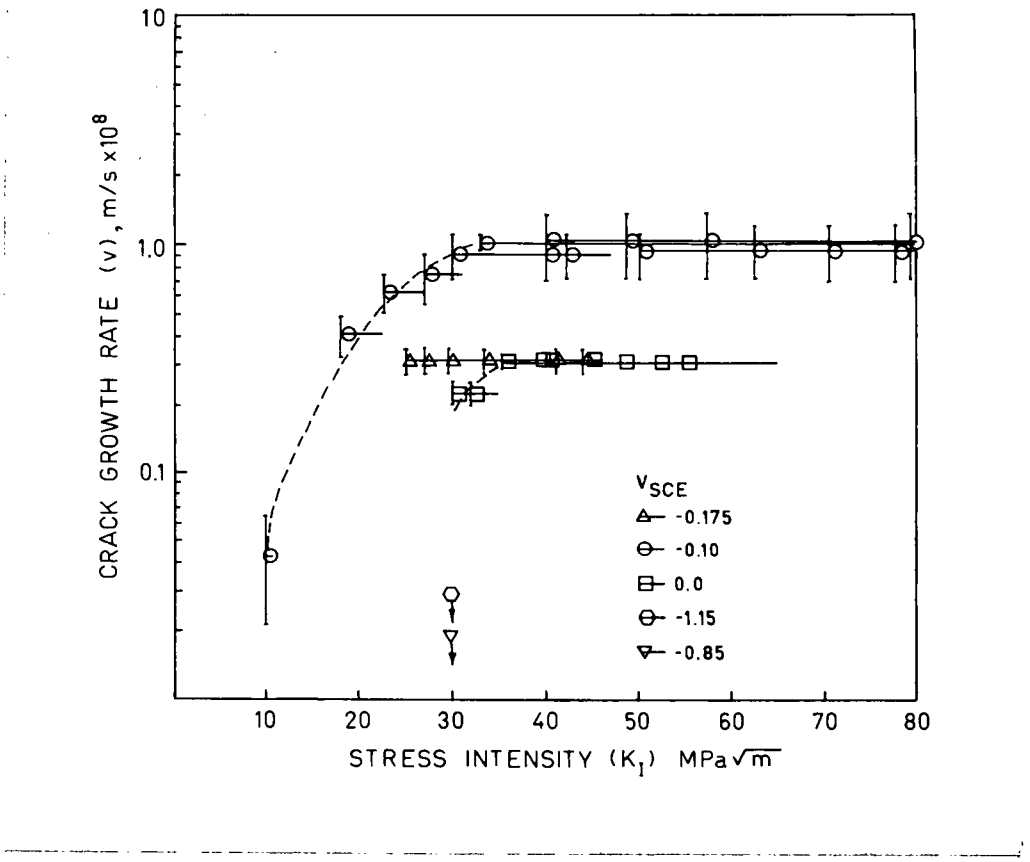

Figure 25 Crack growth rate versus stress intensity at selected potentials in 3.35 mol/kg NaOH, 92 °C.

3.3.0.4 Effect of Cold Work

All of the crack growth rate data in Table III were obtained with 25% cold worked material. Annealed material (no cold work) was also tested at -0.10 V_{SCE} and 92 °C but cracking could not be initiated. The stress intensity could not be increased above 28 MPa$\sqrt{m}$ without considerable deformation of the material. Even after a month, no cracking was observed. Crack growth rate would have been < 1 x 10^{-10} m/s to be undetectable in the test period.

3.3.0.5 Fractography

The crack front was not straight during the tests. Sometimes it led on one face of the specimen, sometimes on the other face, in an apparently random manner.

In all fractographs the cracking direction is from the top to the bottom of the photograph.

Cracking in 3.35 mol/kg NaOH was predominantly intergranular. Figure 26 shows an uncleaned fracture surface of a specimen cracked at -0.10 V_{SCE} and 92 °C. Figure 27 illustrates the effect of increasing stress intensity on the fractography (cleaned). Small areas of transgranular cracking occurred at higher K_I levels as shown in Figure 27c. In Figure 27a there were remnants of corrosion film adhering

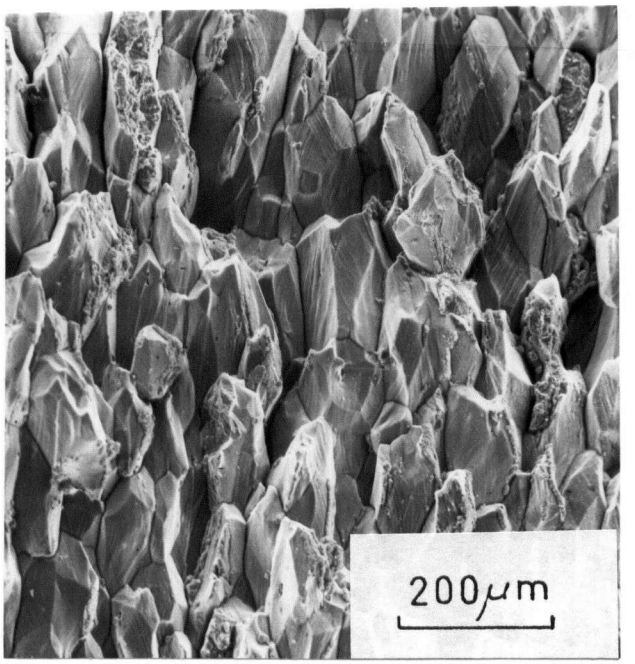

Figure 26 Fracture surface after testing in 3.35 mol/kg NaOH, 92 °C, -0.10 V_{SCE}, 45-47 MPa$\sqrt{m}$.

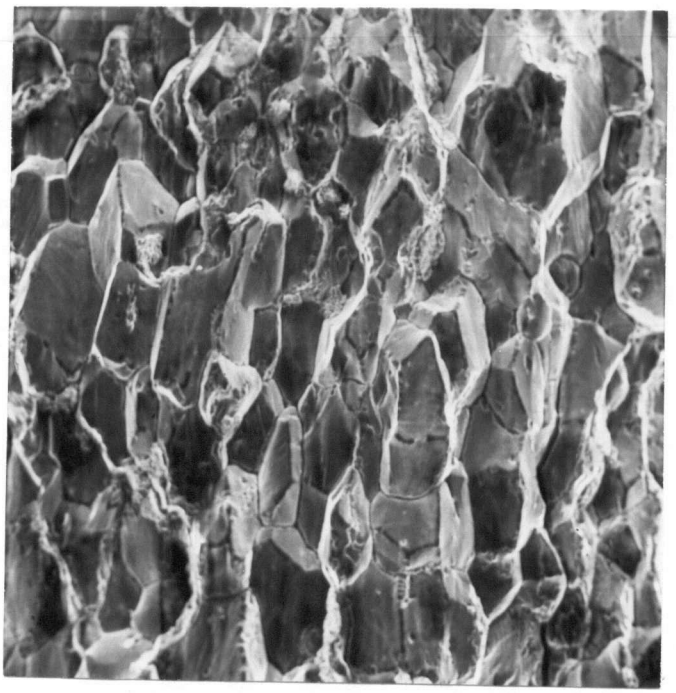

a

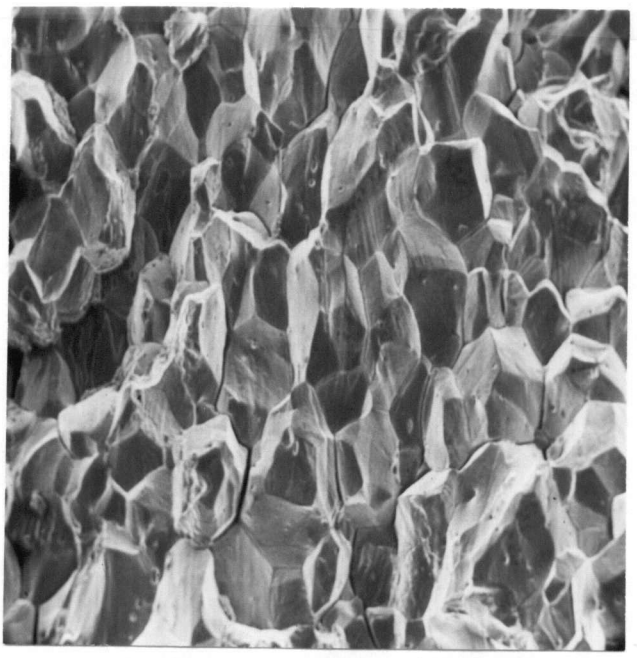

b

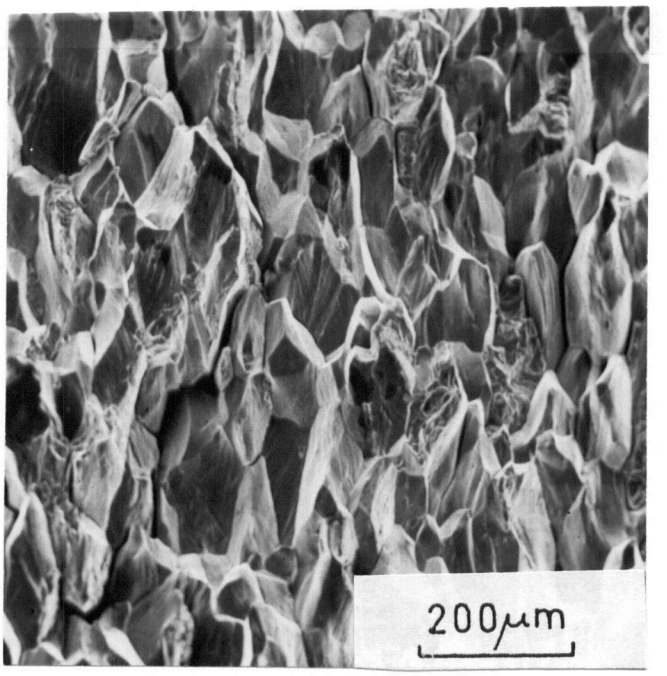

c

Figure 27 Fracture surfaces after testing in 3.35 mol/kg NaOH, 92 °C, -0.10 V_{SCE} at a) 38-40 MPa$\sqrt{m}$, b) 46-48 MPa$\sqrt{m}$, c) 55-60 MPa$\sqrt{m}$.

to the grains; these did not come off during the cleaning (as described in Section 2.3.2).

At stress intensity of about 60 MPa$\sqrt{m}$ crack branching occurred, as seen in Figure 28. Cracks appeared to initiate on the surface in some cases but actually were formed where internal cracks tunnelled beneath the surface and emerged ahead of the main crack.

An interesting aspect of the fractography was the formation of deposits and surface films. At -0.10 V_{SCE}, a fine surface film with the appearance of a straw mat covered the surface, becoming progressively thicker further from the crack front. It was rust red in color. Further along the crack, dark mounds appeared as in Figure 29a. In that area the fracture surface was black. Finally, deposits in a needle-like form were found in the oldest portion of the crack, as shown in Figure 29b.

Comparison of Figure 30 (cleaned surfaces) with Figure 27b shows that there was no significant difference in fractography between 72 and 92 °C when other conditions were held the same.

The fractography was affected by the caustic concentration.

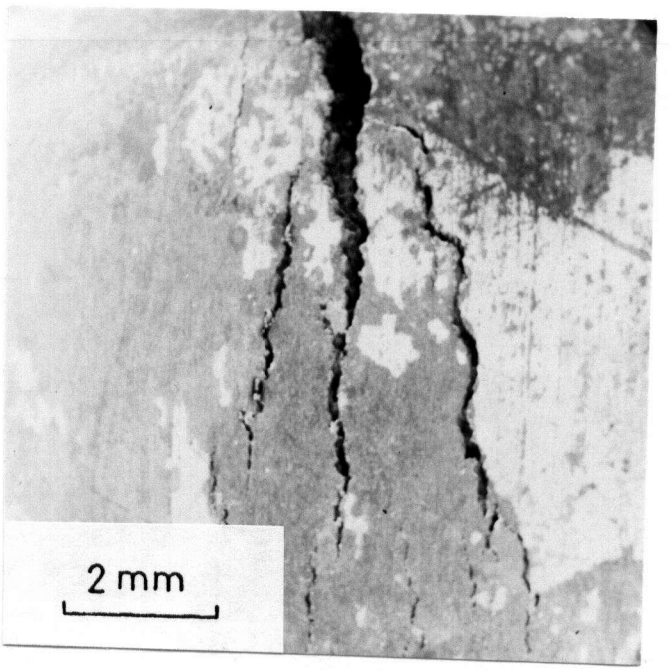

Figure 28 Crack branching. Stress intensity rises from 75 to 105 MPa$\sqrt{m}$ in this view.

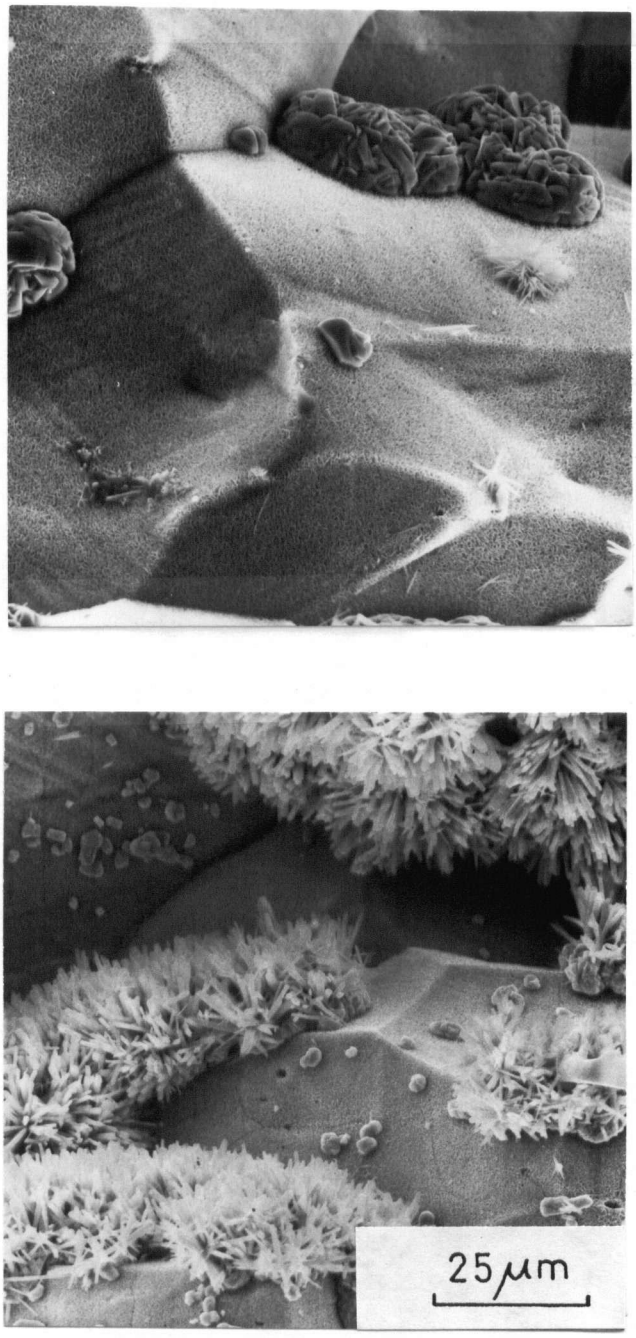

Figure 29 Deposits on fracture surface after testing in 3.35 mol/kg NaOH, 92 °C, -0.10 V_{SCE}.

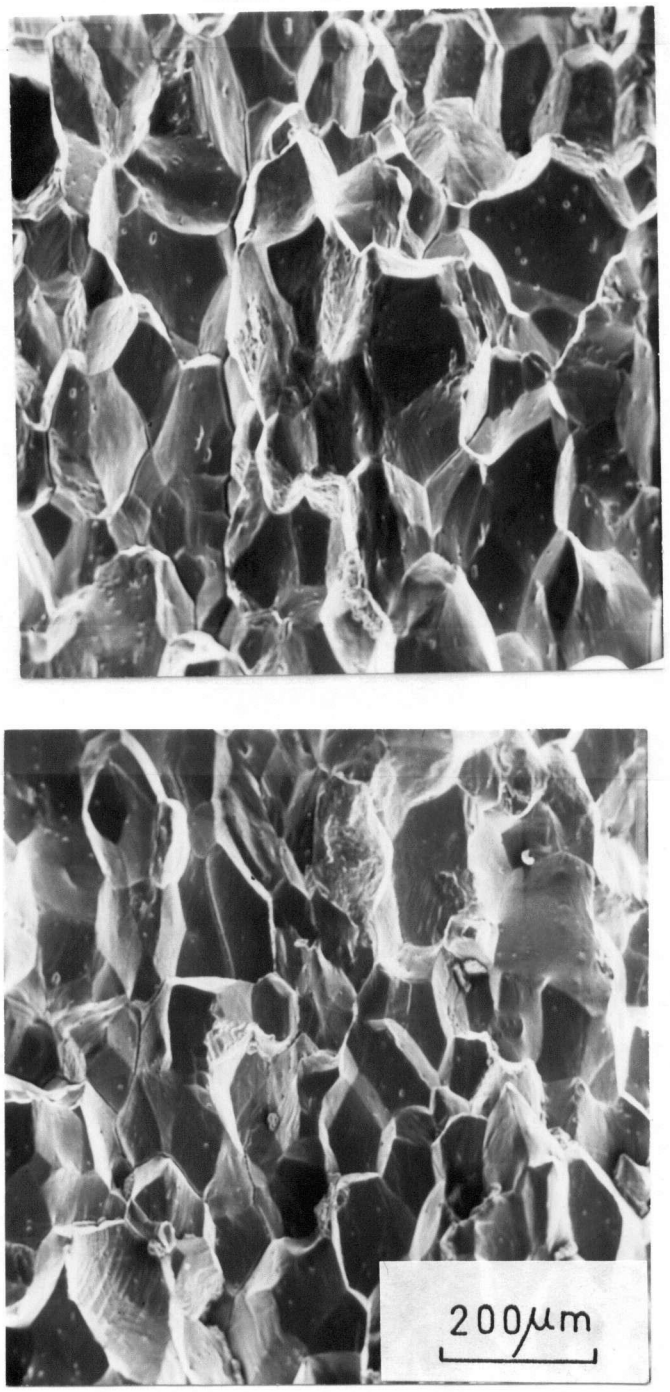

Figure 30 Fracture surfaces after testing in 3.35 mol/kg NaOH, -0.10 V_{SCE}, a) 82 °C 33-34 MPa$\sqrt{m}$, b) 72 °C, 38-40 MPa$\sqrt{m}$.

Figure 31 shows area of transgranular fracture on a specimen tested in 12 mol/kg NaOH. Figure 32, a magnified view of the center of Figure 31, illustrates what may have been a cross-section through several transgranular cracks.

Corrosion deposits on the fracture surface were different in the stronger caustic solution. They were a bronze color near the crack tip and did not exhibit crystalline facets at high magnification. The deposits became brown then black further from the crack tip.

Figure 33 shows the effect of potential on corrosion deposits. As the potential was raised, the density of the deposits increased. When the surfaces were cleaned, the mode of failure was shown to be essentially the same, as can be seen by comparing Figures 34a, 34b and 27a.

3.3.0.6 pH Measurement

Measurements of pH, via indicator paper, showed that the solution which drained out of the crack was the same as that of the bulk solution (i.e. $\sim$ 14 at 25 °C).

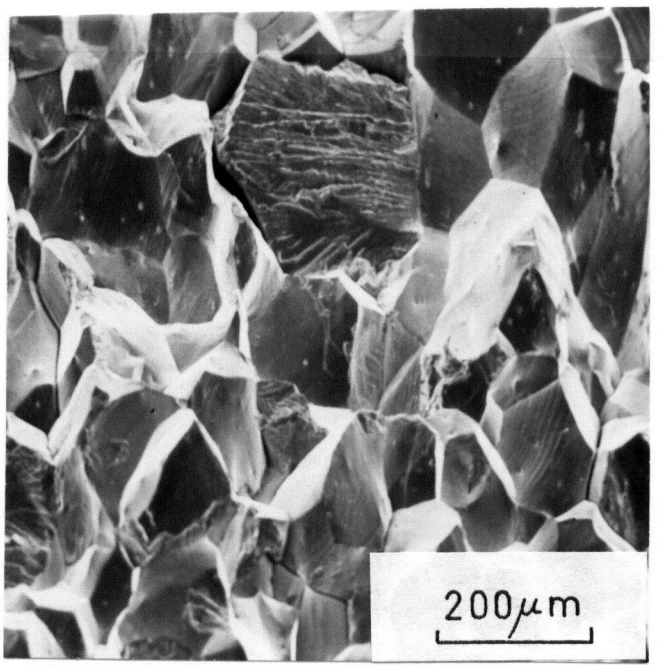

Figure 31 Fracture surface after testing in 12 mol/kg NaOH, 92 °C, -0.10 V_{SCE}, 28-29 MPa$\sqrt{m}$.

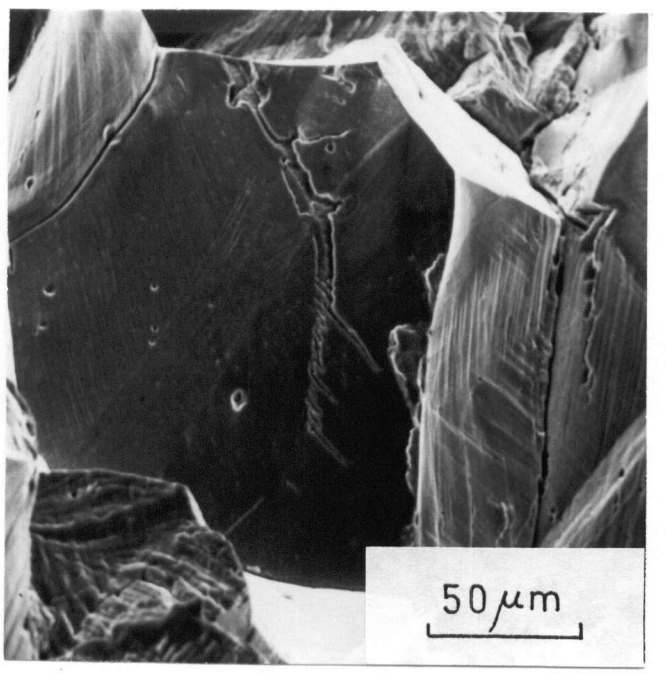

Figure 32 Intergranular facet displaying intersecting transgranular cracking. This is a magnification of the center of Figure 31.

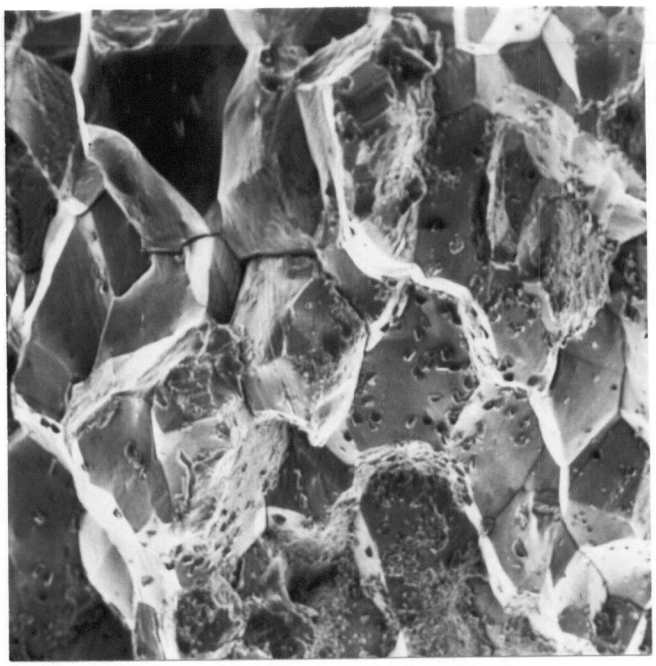

a

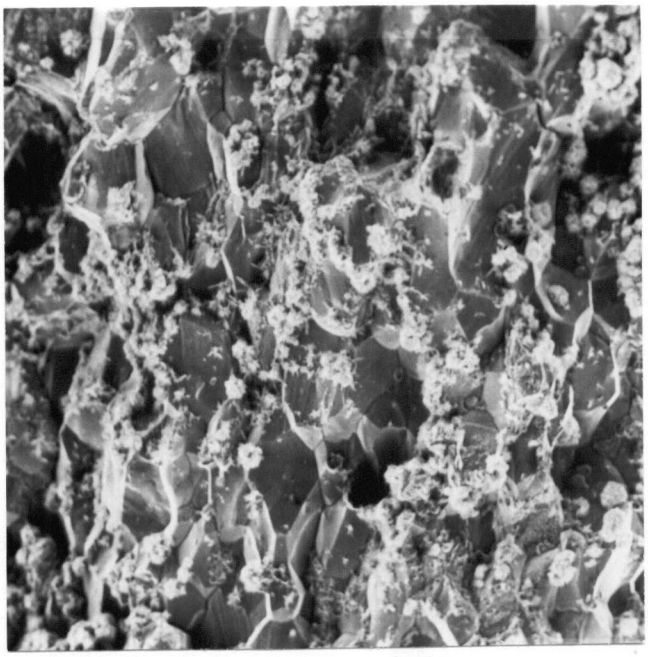

b

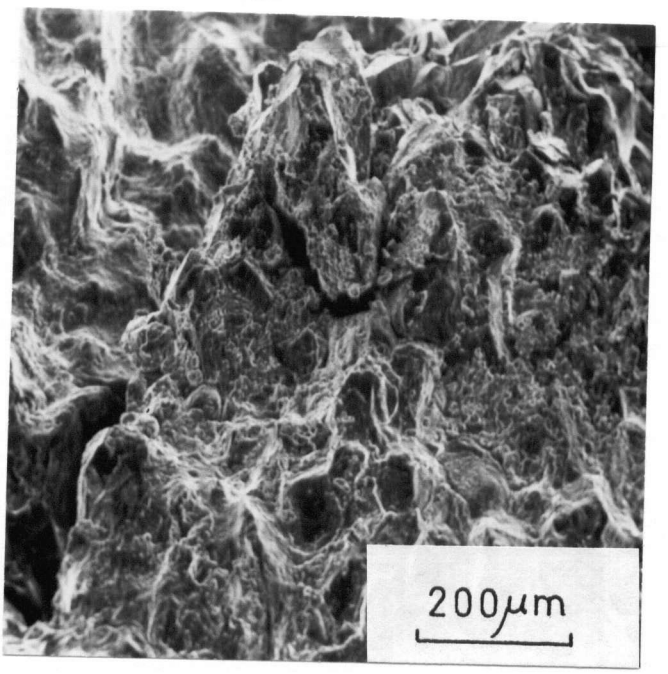

c

Figure 33 Corrosion deposits after testing in 3.35 mol/kg NaOH, 92 °C

a) -0.175 V_{SCE}, 36 MPa$\sqrt{m}$

b) -0.10 V_{SCE}, 42-44 MPa$\sqrt{m}$.

c) 0.00 V_{SCE}, 41-43 MPa$\sqrt{m}$.

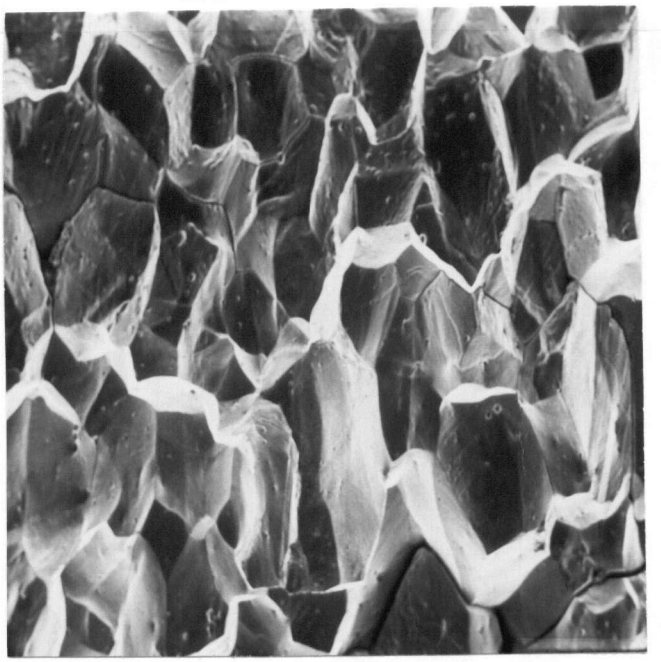

a

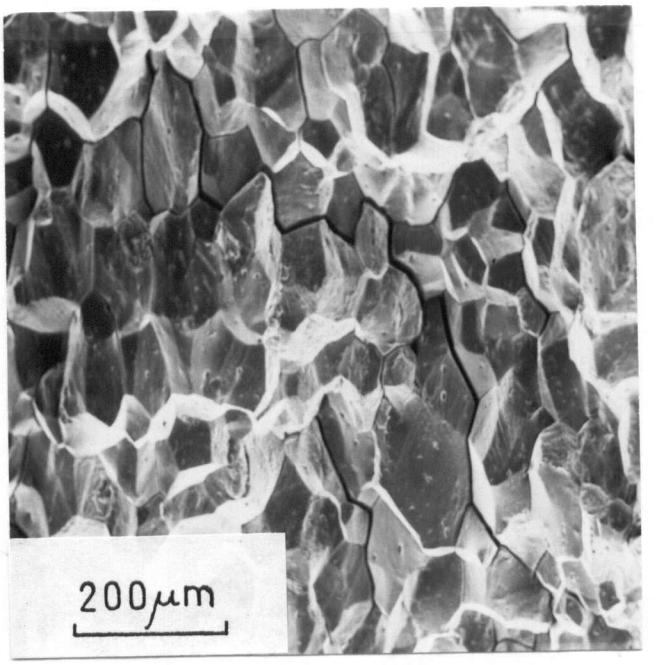

b

Figure 34 Fracture surfaces after testing in 3.35 mol/kg NaOH, 92 °C, a) -0.175 V_{SCE}, 33-35 MPa$\sqrt{m}$, b) 0.00 V_{SCE}, 43-44 MPa$\sqrt{m}$.

3.3.1 $NaOH + Na_2S$

3.3.1.0 2.5 mol/kg NaOH + 0.423 mol/kg Na_2S (Simulated White Liquor)

Fracture mechanics tests were conducted in 2.5 mol/kg NaOH + 0.423 mol/kg Na_2S, 92 °C, at active-passive potentials. One test specimen, at -1.00 V_{SCE} and 30 MPa$\sqrt{m}$, did not crack within 7 days ($v \leq 4.1 \times 10^{-10}$ m/s). Another test was started at -1.10 V_{SCE} and 20 MPa$\sqrt{m}$, but cracking did not occur within 11 days ($v \leq 2.6 \times 10^{-10}$ m/s). The stress intensity was raised to 30 MPa$\sqrt{m}$ for 13 days, with no effect ($v \leq 2.2 \times 10^{-10}$ m/s). Finally, the temperature was raised to 100 °C for 8 days but no cracking was observed ($v \leq 3.6 \times 10^{-10}$ m/s).

3.3.1.1 12 mol/kg NaOH + 0.423 mol/kg Na_2S

Figure 35 illustrates the relation between stress intensity and crack growth rate in 12 mol/kg NaOH + 0.423 mol/kg Na_2S at 92 °C and -1.175 V_{SCE}. The crack growth rate was found to be $(1.48 \pm 0.48) \times 10^{-9}$ m/s for 6 data points between 30 and 37.1 MPa$\sqrt{m}$, and $(2.57 \pm 0.59) \times 10^{-9}$ m/s for 8 data points between 37.1 and 57.9 MPa$\sqrt{m}$. During the test, the potential was raised to -1.15 V_{SCE} for a few days and cracking ceased during that period. Cracking resumed when the potential was reset to -1.175 V_{SCE}. This observation suggested that cracking may occur in the 2.5 mol/kg NaOH + 0.423 mol/kg Na_2S at -1.175 V_{SCE}, even though it did not at

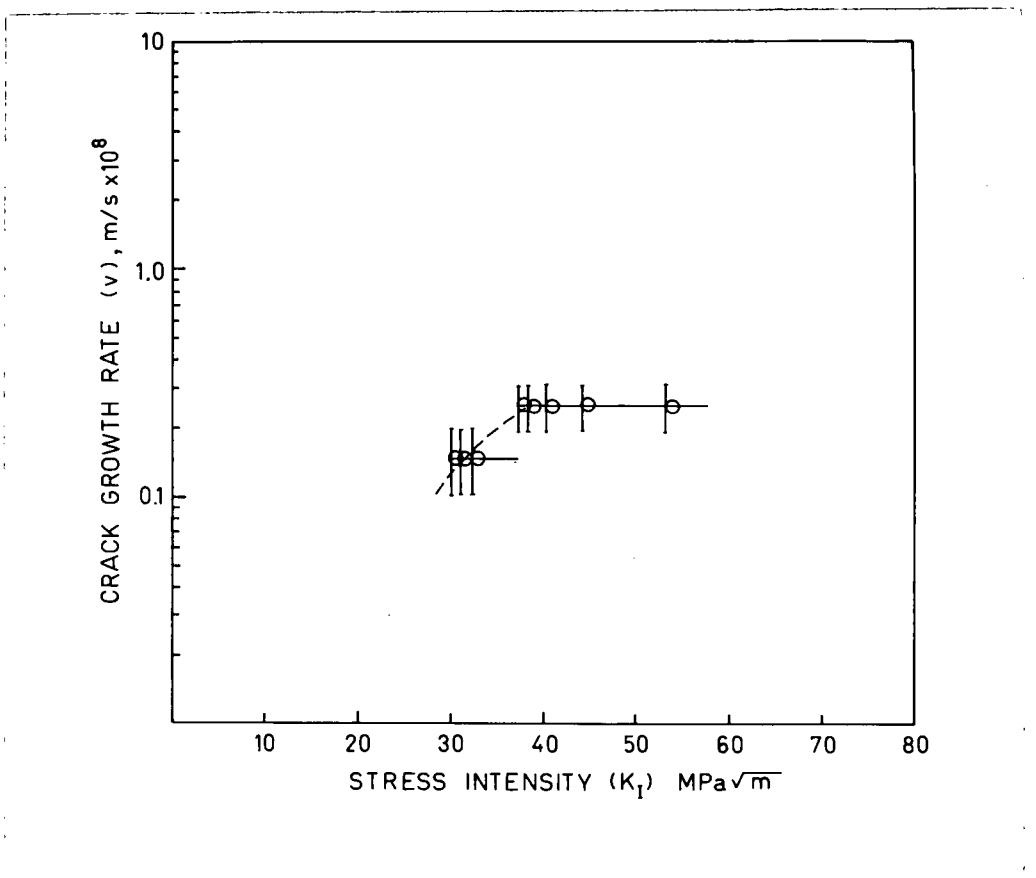

Figure 35 Crack growth rate versus stress intensity in 12 mol/kg NaOH + 0.423 mol/kg Na_2S, 92 °C, -1.175 V_{SCE}.

-1.15 V_{SCE}.

3.3.1.2 Fractography

In all fractographs the direction of crack propagation is from the top to the bottom of the photograph.

The fractography of the specimen cracked in the NaOH + Na_2S solution was mixed transgranular and intergranular. It is illustrated in Figure 36. There was no significant difference in cracking morphology within the range of stress intensity tested. The surfaces were considerably rougher than those obtained in NaOH.

Corrosion deposits shown in Figure 37 were black in color, with a tinge of green when rinsed with distilled water. During removal of deposits in the inhibited acid solution, a hydrogen sulfide smell was produced indicating the deposits were metal sulfides.

3.3.1.3 Solution Appearance

The solution taken from the cell during the test was brown in color. When diluted with the addition of distilled water (i.e. reduction of pH), the solution turned green. Dilution with fresh strong caustic solution did not have this effect.

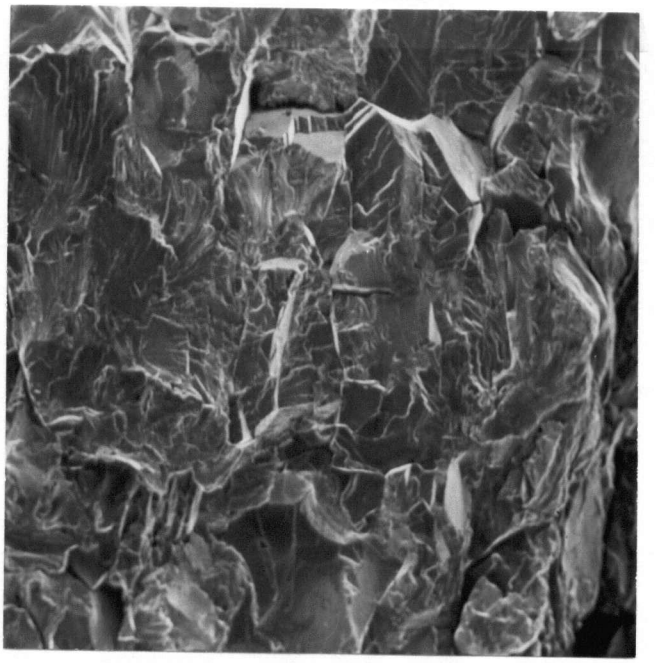

a

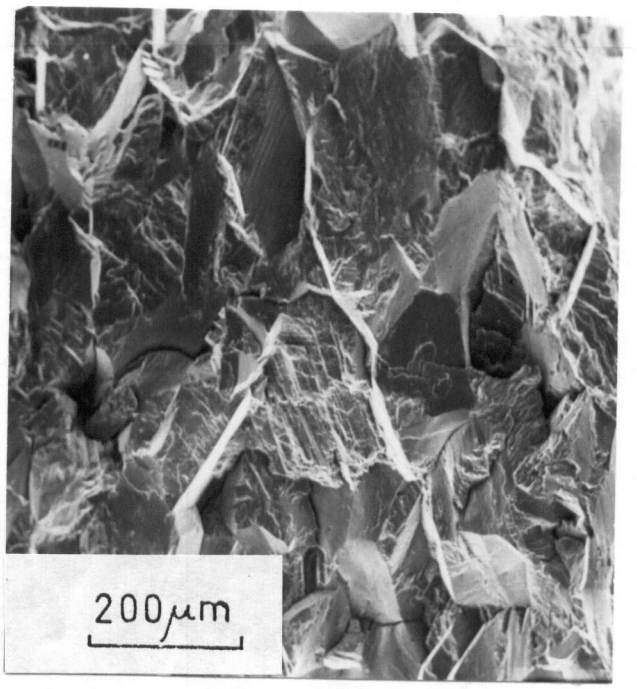

b

Figure 36 Fracture surfaces after testing in 12 mol/kg NaOH + 0.423 mol/kg Na_2S, 92 °C, -1.175 V_{SCE}, a) 37-39 MPa$\sqrt{m}$ b) 50-54 MPa$\sqrt{m}$.

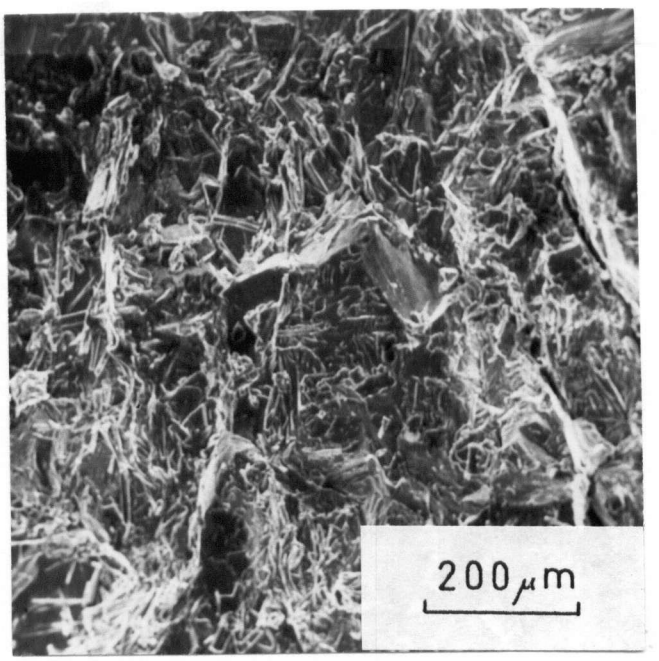

Figure 37 Corrosion deposits after testing in 12 mol/kg NaOH + 0.423 mol/kg Na_2S, 92 °C, -1.175 V_{SCE}, 50-54 MPa$\sqrt{m}$.

3.4 Electron Diffraction Analysis of Surface Films in NaOH

An example of a typical electron diffraction pattern is shown in Figure 38. Table IV is an analysis of the data for this sample. Figure 39 is a plot of D, the diameter of the diffraction pattern rings, versus $\sqrt{h^2+k^2+l^2}$ obtained from the data in Table IV. The lattice parameter, a_o, for the cubic spinel was 8.50 $\pm$ 0.01 Å according to equation 3. The intensities of the diffraction rings were consistent with Fe_3O_4 in the x-ray powder diffraction file[71] and with the intensities calculated for electron diffraction in Fe_3O_4.[72] Other values obtained for the lattice parameter were 8.5 $\pm$ 0.1, 8.8 $\pm$ 0.2, 9.3 $\pm$ 0.3 and 9.3 $\pm$ 0.2 Å.

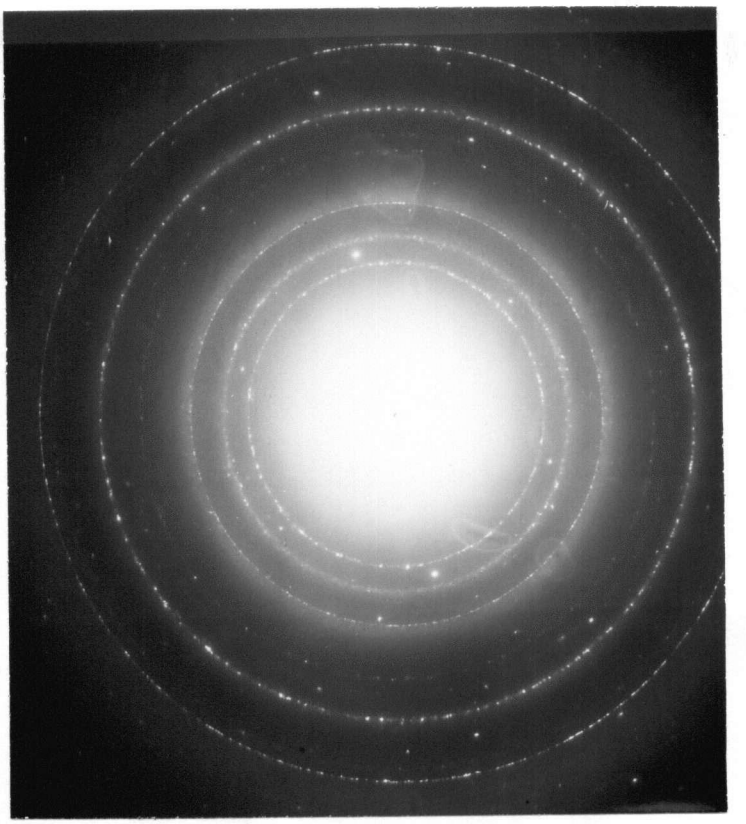

Figure 38 Electron diffraction pattern from corrosion film.

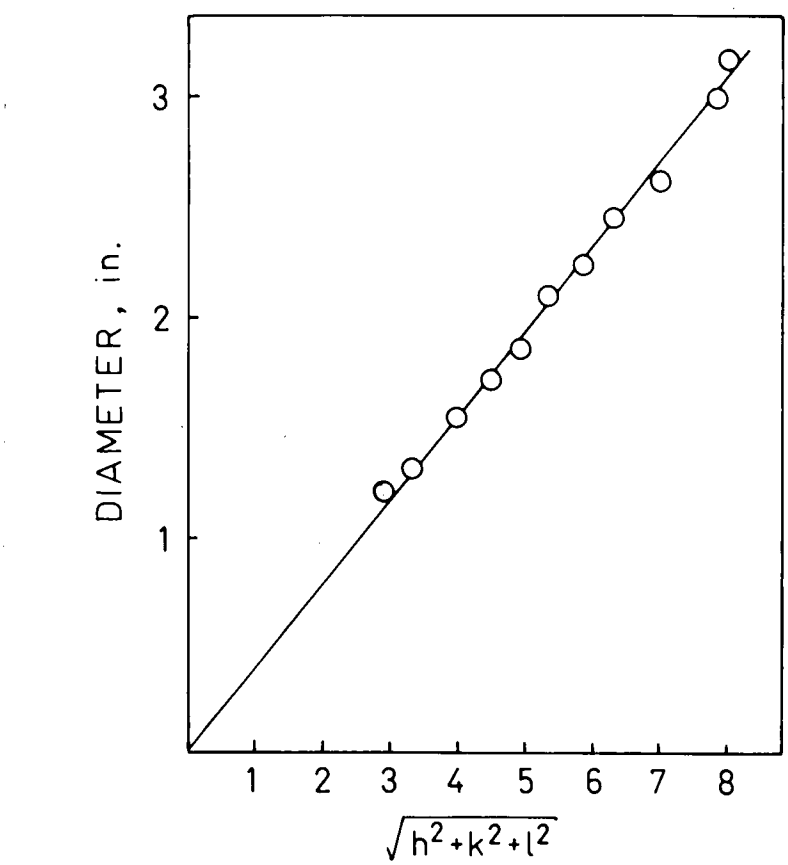

Figure 39 Diameter of diffraction rings versus $\sqrt{h^2+k^2+l^2}$.

Table IV Electron Diffraction Pattern Data

Ring Number	Diameter Inches	d Å	Intensity	h, k, l	$\sqrt{h^2+k^2+l^2}$
1	1.12	2.97	weak	2 2 0	2.83
2	1.22	2.73	spots	-	-
3	1.31	2.54	weak	3 1 1	3.32
4	1.56	2.13	weak	4 0 0	4.
5	1.72	1.94	spot	3 3 1	4.36
6	1.95	1.71	very weak	4 2 2	4.90
7	2.10	1.60	v.v. weak	3 3 3 5 1 1	5.20
8	2.25	1.48	medium	4 4 0	5.66
9	2.44	1.36	spot	6 2 0	6.32
10	2.62	1.27	v.v. weak	5 3 3	6.56
11	2.72	1.22	medium	4 4 4	6.93
12	3.00	1.11	v.v. weak	7 3 1 6 4 2	7.68
13	3.16	1.05	v.v. weak	8 0 0	8.00

4. DISCUSSION

4.1 Interpretation of Anodic Polarization Curves

Electrochemical reactions occurring on the surface may be identified by examining the polarization curves. Anodic current peaks result from reactions which take place to change a metal species to a form more thermodynamically stable at that potential. The thermodynamic stability of a species may be determined from an E-pH diagram, and thus the possible reactions which cause the current peaks may be identified.

The polarization curve for the 316 stainless steel rod material in 3.35 mol/kg NaOH at 92 °C has been presented in Figure 5. It is believed to be a composite curve which may be interpreted in terms of the behavior of the major alloy constituents.

The polarization behavior of chromium was considered with reference to the E-pH equilibrium diagram constructed by Lee[73] for the Cr-H_2O system at 100 °C. The pH is ~12.5-13 in 3.35 mol/kg NaOH at 92 °C.[31] The transpassive region in Figure 9 corresponded to the dissolution of chromium oxide to CrO_4^{2-}.[73] The yellow color of the solution after potentiodynamic scanning in NaOH confirmed the presence of CrO_4^{2-} ions. By inspection, it was concluded that the primary transpassive region observed above -0.25 V_{SCE} in Figure 40 resulted

from formation of CrO_4^{2-}.

The polarization behavior of nickel was analyzed using an E-pH diagram constructed by Cowan and Staehle[74] for the Ni-H_2O system at 100 °C. The increasing current observed above the corrosion potential in Figure 10 may have been due to formation of $HNiO_2^-$ via equation 7.[74]

$$HNiO_2^- + 3H^+ + 2e^- \rightleftharpoons Ni + 2H_2O \quad ...(7)$$

$$E_{HNiO_2^-/Ni} = -0.837-0.074\ pH + 0.037\ \log [HNiO_2^-],\ V_{SHE} \quad ...(7a)$$

The potential of the current peak, -0.85 V_{SCE} was attributed to formation of a passivating film. It was noted that the active-passive peak at -0.85 V_{SCE} for nickel (Figure 10) corresponded to the peak at -0.9 V_{SCE} for the alloy (Figures 5 and 40).

Dissolution of iron to $HFeO_2^-$ via equation 8[75] may have been the major reaction contributing to the active-passive current peak seen in Figure 11.

$$HFeO_2^- + 3H^+ + 2e^- \rightleftharpoons Fe + 2H_2O \quad ...(8)$$

$$E_{HFeO_2^-/Fe} = 0.503-0.111\ pH + 0.037\ \log [HFeO_2^-],\ V_{SHE} \quad ...(8a)$$

The potential of the active-passive transition would be defined by the formation of an oxide film. The current peak observed

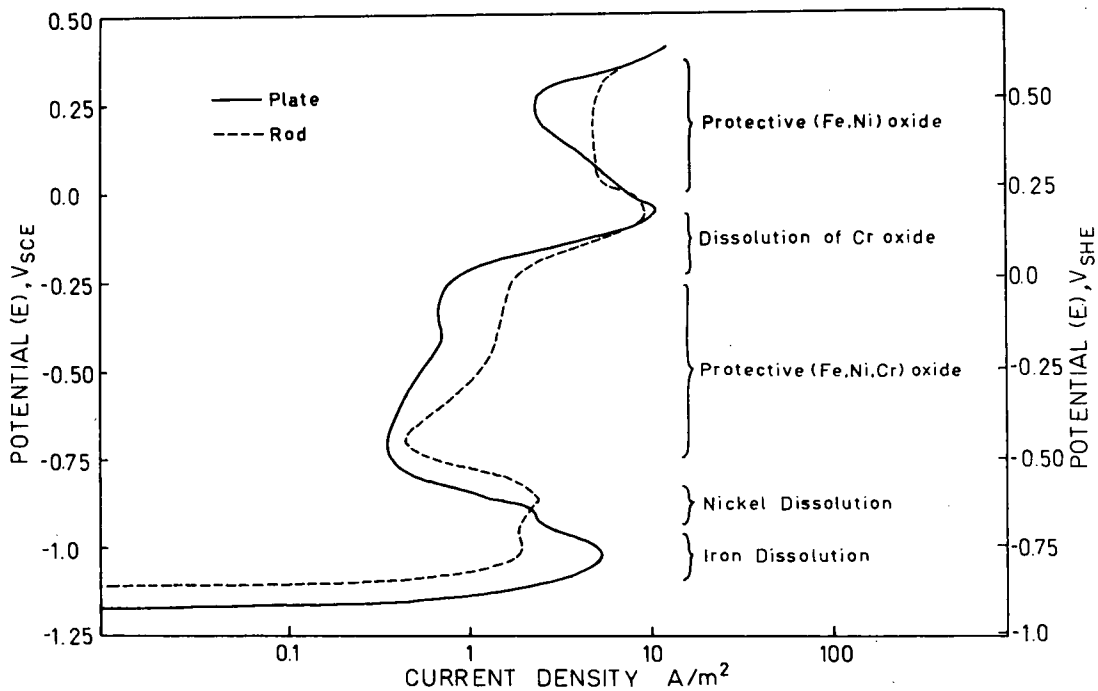

Figure 40 Anodic polarization curves, 316 stainless steel, 3.35 mol/kg NaOH, 92 °C. Identification of reactions.

at -1.05 V_{SCE} on Figure 11 corresponded to the peak at -1.05 V_{SCE} in Figure 40.

Thus, each of the current peaks has been identified with a reaction of one of the major alloy constituents.

Figure 40 illustrates that the active-passive peak due to iron was more pronounced for the plate material. Iron dissolution may have been enhanced by the lower chromium content in the plate material.

The increase in peak current densities as caustic concentration was increased (Figure 7) may be explained using E-pH diagrams. According to the diagrams, iron, nickel and chromium may not passivate at pH 13. However, if the concentration of dissolved species is increased above the 10^{-6} mol/kg concentration assumed for the diagrams then the passivity region may extend to higher pH. To increase the concentration of dissolved species, more dissolution must occur. Thus, in the higher pH solutions higher current densities must be reached before enough dissolution has occurred to provide a concentration of dissolved species adequate to cause passivity.

Increased temperature did not increase the current density significantly (Figure 8) because the thermodynamic stabilities do not change significantly over this range of temperature

as shown by the E-pH diagrams.[73-75]

The polarization behavior of the steel in the NaOH + Na_2S solution has been analyzed by analogy with the behavior in sulfide free solutions due to lack of data on thermodynamics in sulfide solutions.

Figure 41 illustrates how the active-passive current peak observed in the NaOH solution was hidden in the sulfide containing solution. The polarization current in the sulfide solution was the sum of the current of polarization of the steel in NaOH plus current for the oxidation of sulfide. The sulfide may oxidize to thiosulfate[76] via equation 9.

$$S_2O_3^{2-} + 6H^+ + 8e^- \rightleftharpoons 2S^{2-} + 3H_2O \qquad ...(9)$$

$$E_{S_2O_3^{2-}/S^{2-}} = 0.034-0.056\ pH + 0.0093 \log\left([S_2O_3^{2-}]/[S^{2-}]\right), V_{SHE} \qquad ..(9a)$$

The reversible potential of equation 9, -0.959 V_{SCE}, was calculated after Tromans[61] using the average pH value given by Singbeil.[49] Hence, the polarization behavior of the steel was hidden at > -0.75 V_{SCE} by oxidation of sulfide.

Biernat and Robins[75,76] have constructed E-pH diagrams for the Fe-S-H_2O and S-H_2O systems at 100 °C. According to their data, iron sulfides are stable at low potential.

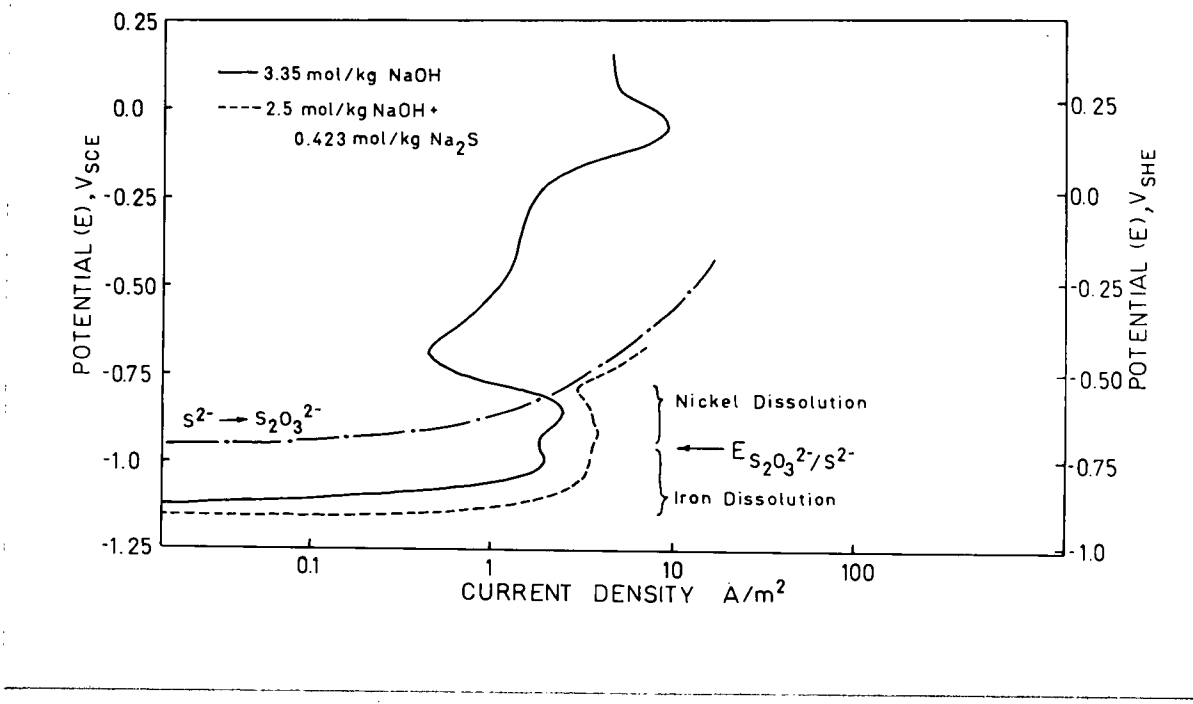

Figure 41 Anodic polarization curves, 316 stainless steel, NaOH + Na_2S, 92 °C. Identification of reactions.

Similarly, MacDonald and Syrett[77] have constructed an E-pH diagram for the Ni-S-H_2O system at 25 °C, indicating possible formation of nickel sulfides at low potential. No E-pH diagram was available for the Cr-S-H_2O system.

For higher concentrations of NaOH, larger peak anodic current densities were observed (Figure 13). Similar peaks have been observed for mild steel.[49,61,62] The position of the major current peak has been attributed to deposition of FeS when its solubility product is exceeded.[61]

4.2 SCC Susceptibility

Comparison of the slow strain rate tests with polarization behaviour indicated that SCC susceptibility in NaOH solution was associated with instability of the passive film. The polarization study showed that breakdown of passive film and dissolution to chromate occurred in the primary transpassive region where SCC susceptibility was greatest (Figure 15).

The surface of a specimen tested in the susceptible potential range was deeply cracked (Figure 16). The cracks may have formed where the surface film was broken, thus allowing fast localized dissolution. Rupture of the film may have occurred by the sudden release of dislocations piled up behind the film. According to the film rupture and dissolution model,[19] the released dislocations would form a slip

step of bare metal which would then be dissolved. Formation of chromate ions would have caused rapid dissolution resulting in formation of deep cracks before repassivation with an iron-nickel film could occur.

A SCC mechanism involving hydrogen embrittlement would be ruled out at primary transpassive potentials. In pH 12.5 solutions, hydrogen evolution[75] via equation 10 would occur only below -1.17 V_{SCE}.

$$2\,H^{+} + 2e^{-} \longrightarrow H_2 \qquad \ldots(10)$$

$$E_{H^{+}/H_2} = 0.057 - 0.074\ pH - 0.037 \log a_{H_2} \qquad \ldots(10a)$$

A pH measurement of solution draining out of a stress corrosion crack in a fracture mechanics specimen showed that pH was not measurably lower in the crack solution than in the bulk solution. Thus local hydrogen evolution was unlikely even inside cracks.

In contrast to behavior of mild steel in NaOH solutions,[49] the 316 stainless steel showed no susceptibility to SCC at the active-passive potential. The absence of susceptibility at these potentials may have resulted from a number of factors. No significant film instability may occur in this range. A stable chromium film may minimize dissolution of iron and

nickel and thus prevent instability. An alternate factor causing the absence of susceptibility may have been that the strain rate was too high. In that case, failure would have occurred before cracking had had time to progress.

If cracking in the slow strain rate tests occurred by cycles of film rupture, dissolution and repassivation then the rate and duration of dissolution and repassivation cycles would have affected the cracking rate. The low current density at the active-passive peak indicated that dissolution rate was relatively low at this potential. Very little dissolution might have taken place before repassivation was complete. Time in the dissolution stage would have been decreased by rapid repassivation kinetics, perhaps reducing dissolution below that required to sustain cracking. Additionally, if hydrogen embrittlement were important in the cracking mechanism at this potential, then rapid repassivation might reduce the period during which hydrogen is absorbed into the lattice.

Park et al.[8] have explained SCC of 304 stainless steel in 20N NaOH in terms of the ratio of current density on a bare metal surface to that on a filmed metal. This ratio was lowest in the primary transpassive region. Although they observed cracking near the corrosion potential ($\sim$-0.9 V_{SHE}), the rate of cracking was lower for alloys with higher chromium

content. The present investigation differed from that of Park et al. in that cracking was not observed in NaOH solutions at the corrosion potential. The difference may have been due to their more concentrated solutions, faster strain rate, and different alloy composition.

Santarini[78] tested a 17 Cr-13 Ni steel in 50% NaOH at 130 °C. During the test, the open circuit potential rose from -1.17 to -1.13 then -1.00 V_{SCE}. This was in the potential regime where iron in the alloy would be dissolving, chromium would form a passive film and nickel would be thermodynamically stable. Santarini identified this region as dangerous for SCC. The same result was not observed in the present study, perhaps because of the lower temperature and concentration here. Also, the present study was potentiostatic and so would not allow a shift in potential, as was observed by Santarini and included in the model he proposed.

In the 2.5 mol/kg NaOH + 0.423 mol/kg Na_2S (simulated white liquor) solution, susceptibility to SCC was detected by SSRT at -1.15 to -1.175 V_{SCE}. According to equation 10, H_2 may be evolved at this potential. The presence of S^{2-} ions may retard the hydrogen evolution and so promote absorption of adsorbed hydrogen. This dissolved hydrogen may then diffuse into the metal to cause hydrogen embrittlement. The effect of sulfide (H_2S solution) in poisoning the recombination

reaction 10 has been shown experimentally.[79]

The sulfide also may have weakened the passive surface film formed at this potential, making it less protective and thus allowing dissolution to occur. Another possibility may be that the sulfide affected the repassivation rate. S^{2-} may have adsorbed onto the surface instad of OH^-, thus reducing the rate of formation of passive film and slowing repassivation. The slower repassivation rate may leave the surface bare for a longer period of time. This bare surface may catalyze evolution of adsorbed hydrogen thereby leading to greater hydrogen absorption as shown by Berkowitz and Horowitz.[79]

Sensitization caused some susceptibility in 3.35 mol/kg NaOH at -1.15 V_{SCE} in the slow strain rate tests (Figure 15). The sensitization would have tied up some of the chromium in intergranular carbides and hence the film may not have formed properly adjacent to grain boundaries. Lower chromium content may also have resulted in slower repassivation thus allowing more dissolution before repassivation was complete. Alternately, slower repassivation kinetics might allow longer time for a hydrogen embrittlement mechanism to be operative.

Sensitization did not affect susceptibility in the NaOH + Na_2S solution. Perhaps it showed no effect because sulfide had already slowed the repassivation kinetics.

An annealed SSRT specimen tested at the transpassive potential in NaOH solution had a larger percent reduction in area at failure than did an as-received specimen. The annealed material was softer than the work-hardened as-received material. Critical strains would not have developed in the material until later in the test when elongation was greater. Annealed specimens tested at non-susceptible potentials might have

showed higher percent reductions in area, too. The result with the annealed specimen indicated that stress relief may reduce susceptibility but does not necessarily prevent SCC.

4.3 Crack Growth Rates and the Mechanism of Cracking

SCC susceptibility was greatest in the potential regions indicated by the slow strain rate tests, and these regions were correlated to potential ranges for film instability by means of the polarization curves. Cracking was attributed to the operation of a film rupture and dissolution mechanism. As described below, a study of the crack growth rates under a variety of conditions provided conclusive evidence regarding the nature of the dissolution mechanism.

4.3.1 Potential Dependence of Crack Growth Rate

Fracture mechanics testing confirmed the SSRT result that SCC susceptibility was potential dependent.

In the 3.35 mol/kg NaOH, Region II crack growth was slower at 0.0 and -0.175 V_{SCE} than at -0.10 V_{SCE} (Figure 25). This result was expected because 0.0 and -0.175 V_{SCE} were at the extremities of the region of SCC susceptibility determined by SSRT. Fracture mechanics tests at -0.85 and -1.15 V_{SCE} confirmed the absence of cracking at active-passive potentials in the 3.35 mol/kg NaOH.

The cracking in sulfide containing solutions was potential dependent, also. The cracking observed in 12 mol/kg NaOH + 0.423 mol/kg Na_2S at -1.175 V_{SCE} was stopped when the potential was raised to -1.15 V_{SCE}. Specimens tested in 2.5 mol/kg NaOH + 0.423 mol/kg Na_2S did not crack at -1.00 or -1.10 V_{SCE}. The SSRT results indicated some SCC susceptibility at $\sim$ - 1.15 V_{SCE} but this was not observed for the fracture mechanics specimens made from plate material. Perhaps the difference was due to different compositions of the rod and plate, mainly of chromium and nickel. Alternately, the relatively high percent reduction in area at active-passive potentials may have indicated marginal SCC susceptibility, which was insufficient to initiate cracking in the fracture mechanics specimens.

Thus, the investigation of potential dependence of crack growth rate indicated that the slow strain rate tests and fracture mechanics tests were consistent and that crack growth rate was fastest in those potential ranges of greatest susceptibility to SCC as predicted by SSRT.

4.3.2 Dissolution Rate and Crack Growth Rate

Fracture mechanics tests provided crack growth rates in Regions I and II of the v - K_I plots. K_I independent cracking kinetics in Region II were the result of stress independent processes only, of which dissolution is the most probable.

An attempt was made to relate the crack growth rate to the dissolution rate via Faraday's law.[80]

$$v = \frac{i_a W}{F \rho} \qquad \ldots(11)$$

where

v = crack growth rate

i_a = anodic current density

W = equivalent weight of the metal

F = Faraday (9.65×10^4 A·S)

ρ = density of metal

The anodic current densities, i_a, were obtained from the polarization curves. At -0.10 V_{SCE} the current density for dissolution of chromium was much larger than that of iron or nickel (Cr: 14.3 A/m^2, Fe: 2.0 A/m^2, Ni: 0.3 A/m^2). The crack velocity calculated from the anodic current density for dissolution to Cr(VI) was: 1.79×10^{-10} m/s. Similarly for iron to Fe(III) the calculated crack growth rate was 0.49×10^{-10} m/s and for nickel to Ni(II) it was 1.02×10^{-11} m/s. Crack growth rate in sulfide solution was not compared with expected crack growth rate calculated from dissolution rate because of uncertainty about what species would be formed; or what their dissolution rates would be.

None of the calculated crack growth rates was large enough to account for the observed rate in NaOH ($\sim 1 \times 10^{-8}$ m/s).

However, during cracking, dissolution would not have been occurring uniformly over the surface, but would have been concentrated at defects in the oxide film. Therefore, the true current density at defect sites would have been much higher than that indicated by the polarization diagrams.

Park et al.[8] have shown that current density on a bare stainless steel electrode in NaOH is about 100 times that on a filmed electrode. This is corroborated by Hoar and Jones[91] for mild steel straining in NaOH, and by Diegle and Vermilyea[82] for iron in NaOH using a drop weight apparatus. If current densities on straining electrodes are 100 times higher than on static electrodes, then cracking rates may be also. This would account for the observed cracking rates.

It has been concluded that the magnitude of crack growth rate cannot be calculated from the magnitude of the current density on the polarization diagram. However, increases in anodic current density still may correlate with increases in crack growth rate. In 3.35 mol/kg NaOH at -0.10 V_{SCE}, increases in crack growth rate over a range of temperature (Figure 21) correlated with increases in current density (Figure 8). At 92 °C, crack growth rate (Figure 24) correlated with increase in current density over a range of potentials (Figure 7).

It already has been shown that the crack growth rates are qualitatively consistent with a dissolution mechanism. Unfortunately, comparison of current densities on polarization curves have been shown to be inadequate for quantitatively predicting crack growth rates. Current densities were consistent with a localized dissolution mechanism but neither confirmed it nor revealed the nature of the dissolution process.

4.3.3 Kinetics of Crack Growth Rates

The apparent activation energy for crack growth rate was found to be $\sim$60 kJ/mol in 3.35 mol/kg NaOH and $\sim$37 kJ/mol in 12 mol/kg NaOH (both at -0.10 V_{SCE}). These apparent activation energies were consistent with a dissolution process controlled by charge transfer, for which values may range from 21-105 kJ/mol.[83] The apparent activation energies were too large to result solely from control by diffusion (transport) in the liquid phase.

An attempt was made to correlate the apparent activation energy for cracking with that of the dissolution current measured on the polarization diagram (Figure 8). The activation energy varied from 93.8 $\pm$ 33.1 kJ/mol at -0.10 V_{SCE} through 66.8 $\pm$ 19.9 kJ/mol at the primary transpassive current peak to 33.9 $\pm$ 3.8 kJ/mol at the secondary passive minimum. The fact that the activation energy of the current peak gave the best correlation with the apparent activation energy for crack growth rate supports the film rupture and dissolution

model in which the magnitude of the transient dissolution current peak may greatly affect crack growth rate.

The apparent activation energy in the 3.35 mol/kg NaOH solution was indicative of charge transfer while that in the 12 mol/kg solution was more representative of the lower values obtained in mixed charge transfer-diffusion control.[49] In the 12 mol/kg solution, diffusion may play a greater part in the mixed charge transfer-diffusion control of dissolution.

Insufficient data precluded calculation of an activation energy for cracking in sulfide solutions.

The values of activation energy obtained were consistent with results obtained in other environments by other investigators. Russel found an apparent activation energy of 67 kJ/mol for 25% cold worked 316 stainless steel from the same plate used in the present study.[14,48] Speidel, testing 304 stainless steel in 22% NaCl solution found an apparent activation energy of 72 kJ/mol.[13] Staehle obtained 42-75.3 kJ/mol for nickel straining and static electrodes in 1N H_2SO_4.[84] The lower activation energy of straining electrodes was attributed to 'lattice disarray' after Hoar[85] who predicted that there might be a reduction in the activation energy for metal dissolution due to an increase in the internal energy of atoms in rapidly emerging slip "pockets."

Petit[86] studied the transpassive behavior of nickel in solutions of sulfuric acid and sodium sulfate. He determined the activation energies of the reaction rates (equivalent to currents at the transpassive peak or in the secondary passive region). Impedance measurements showed that the reactions occurred in several stages. The activation energies quoted were 50.5-70.0 kJ/mol at a polarization rate of 33 mV/min.

Staehle[16] has suggested that the current transient associated with corrosion of film-free metal following film rupture is related to the rate of crack propagation. He presented results that showed activation energies for 'partial currents', and that the activation energy increased with nickel content. Thus nickel would reduce cracking rate by reducing the size of the current transient following rupture, and chromium would increase the cracking rate by increasing the size of the current transient.

4.4 Fractography and the Dissolution Mechanism

4.4.0 Corrosion Deposits

The corrosion deposits shown in Figure 29 appear to have precipitated from solution. The presence of these crystalline deposits indicated that the solution within the crack was saturated with metal species. Unfortunately the composition of the deposits could not be determined. The crystalline deposits in Figure 29b resembled hematite

platelets observed on iron in NaOH solutions.[87]

At higher temperatures, where cracking was faster, the deposits were slightly thicker. The faster dissolution at the higher temperatures may have carried more ions into solution, and these subsequently may have precipitated to form the thicker deposit. These precipitates appeared to have formed during cracking. They were thicker near the crack mouth where the fracture surface had been exposed longer, thus allowing a longer time for precipitation to occur.

The corrosion deposits were affected significantly by potential. Deposition was greater as the potential was increased from -0.175 to 0.0 V_{SCE} (Figure 33). This may have been the result of transition from passive to secondary passive film. It may also have reflected differing deposition resulting from the different equilibrium concentrations for soluble species at these potentials. The heavy deposits at 0.0 V_{SCE} may have interfered with diffusion processes over distances smaller than a grain.

Heavy deposition was found in the 12 mol/kg NaOH solution. The control potential was in the secondary passive region. Corrosion deposits were thicker than those found at the same potential in the 3.35 mol/kg NaOH, thus indicating that diffusion may have been affected in the stronger NaOH solution.

Indeed, the apparent activation energy confirmed this, being a low value which was consistent with mixed activation-diffusion control.

Corrosion deposits were also found in the sulfide containing solutions. The observation of metal sulfides on the fracture surfaces was in agreement with previous observations of iron sulfide formation on iron in NaOH + Na_2S solution.[61] As previously stated, solution taken from the cell during the test turned green when neutralized with the addition of distilled water. Taylor and Shoesmith[88] have studied green alkaline sulfide solutions of pH 12-13 and have determined that the green color is derived from colloidal $NaFeS_2$ in solution. This was evidence that iron dissolved during the fracture mechanics tests. The formation of these deposits would however not rule out hydrogen embrittlement at this potential as the deposits may have formed by dissolution from the crack walls.

4.4.1 Fracture Mode

The cracking progressed mostly in an intergranular mode. Intergranular segregation may have been a factor in the faster dissolution at grain boundaries.[89] Another factor causing the intergranular cracking may have been that strain was concentrated there. Dislocation pile-ups at the grain boundaries may have resulted in a greater strain rate in the adjacent area

when released. Slip bands were observed on the grain surfaces in Figures 26-33, offering evidence that substantial straining took place there. Larger and more numerous slip steps resulting from this straining would have provided sites for greater dissolution at the grain boundaries. The grain boundaries themselves may have increased the dissolution rate due to their inherent local atomic disarray. The disarray may have increased the rate of adsorption of damaging species by offering an increased number of surface imperfections at which adsorption could take place. This adsorption may have stimulated faster dissolution.

At the primary transpassive potentials, adsorption may have been essential to the dissolution process. Knoedler and Heusler[90] have suggested that the oxidation of chromium to CrO_4^{2-} proceeds via six consecutive charge transfer reactions. The intermediates cover the surface with an adsorbed monolayer. Most of the surface is covered with Cr(IV), its oxidation being the rate determining step. The reactions are summarized by equation 12.

$$Cr(OH)_{x+1} + e^- \rightleftharpoons Cr(OH)_x + OH^- \qquad ...(12)$$

The fractography that was observed in this study was consistent with OH^- adsorption, and thus supported the dissolution mechanism suggested by Knoedler and Heusler.

Figure 27 illustrates the effect of stress intensity on fractography. Transgranular cracking was observed only at high stress intensity in 3.35 mol/kg NaOH. The greater amount of deformation at this high stress intensity may have provided competing sites within the grain either by severe disruption of oxide film or high strain energy sites for adsorption. This observed effect was opposite to the results of Russel[48] for 316 stainless steel in $MgCL_2$. A decreasing fraction of transgranular SCC and increasing intergranular SCC were observed as K_I was increased in $MgCl_2$. The different behavior observed by Russel may have resulted from different temperature, potential, pH, or by the presence of Cl^-. Metallurgical differences could be ruled out as the plate and preparation of specimens were the same as for the present studies. If grain boundary segregation effects were important to the intergranular failure in caustic, they obviously had a different effect in $MgCl_2$.

In the NaOH solutions, there was no change in the mode of cracking over the range of primary transpassive, transpassive peak, and secondary passive potentials investigated. Beyond this range, cracking mode may change. Some evidence in the literature supports this possibility. Okada et al.[27] have quoted a study by Subramanyam and Staehle which showed that cracking mode depended on electrode potential. At transpassive potentials, intergranular cracking was favored in 304 stainless

steel in 70% NaOH but at the active-passive potential transgranular cracking predominated.

The cracking mode in NaOH solutions did not change with temperature (Figures 26 and 30) in spite of the substantial range of crack growth rate. The absence of an effect indicated that change in cracking mode at high K_I values at 92 °C was not due to higher crack growth rate at those higher stress intensities.

Caustic concentration affected the mode of cracking. Figure 31 illustrates that some transgranular cracking occurred in 12 mol/kg NaOH perhaps when the orientation was favorable. A clue to understanding the change in fractography with concentrations might be found in the value of the activation energy. That value suggested that in the concentrated solution, diffusion was playing a larger role in mixed control of dissolution. This may in turn have affected the fractography. Surface imperfections at grain boundaries which may have been important in increasing dissolution rate for activation controlled dissolution may have been less important in a cracking process already slowed down by diffusion influences. Thus transgranular cracking could be as favorable as intergranular.

In contrast to the intergranular cracking in the NaOH, the fracture surfaces in the 12 mol/kg NaOH + 0.423 mol/kg Na_2S solution exhibited mixed intergranular-transgranular

cracking. The larger proportion of transgranular cracking in the sulfide containing solution than in the straight NaOH solution may have resulted from the presence of the sulfide ions. The sulfide may have adsorbed on the lattice imperfections at the grain boundaries thereby decreasing the adsorption of OH^- and lessening the dissolution rate at the grain boundaries. If adsorption of S^{2-} reduces dissolution rate then, similarly, it may be responsible for the slower crack growth rate in the NaOH + Na_2S solution.

Alternately, the difference in fractography may have resulted from testing in a much different potential range. Hydrogen embrittlement was possible at this potential and may have caused the transgranular cracking. S^{2-} may have been important in causing hydrogen embrittlement by poisoning hydrogen recombination. Lack of experimental results at these conditions has precluded evaluation of this possibility.

In contrast to the present result, Asaro[34] found that 304 stainless steel showed mostly intergranular cracking in 50% NaOH with 0.03 mol/liter Na_2S at 180 °C. The difference may have resulted from either lower S^{2-} concentration or different potential (unknown).

4.5 Electron Diffraction Analysis of Surface Films in NaOH

The electron diffraction ring patterns were consistent

with a spinel type of structure[71,72] but the lattice parameters were generally a little higher than that expected from published data for Fe-based spinels[91] e.g. 8.50 Å versus ~ 8.38 Å for Fe_3O_4. The difference may have been due to a different valency state or an irregular lattice arrangement here. Nikiforuk[70] obtained reasonable values for spinel lattice parameters formed on stainless steels in $MgCl_2$ using the same method.

There were some fundamental problems with this method of analysis. The film analyzed was not a representative sample of the film on the fracture surface. Much of the surface deposit was thick and as such was opaque to electrons. The patterns may not have been for material from the fracture surface but from the sides of the specimen. The method described by Birley[72] for obtaining electron diffraction patterns from the unstripped fracture surface would avoid these problems. In that method, the electron beam passes through oxides on surface asperities.

The surface film was tentatively identified as Fe_3O_4. E-pH diagrams indicate that FeOOH might be formed at primary transpassive potentials. The FeOOH may have dehydrated on removal from the solution or in subsequent handling to form HFe_5O_8 (γ-Fe_2O_3)[92] via:

$$5\ FeOOH \rightarrow HFe_5O_8 + 2H_2O \qquad \ldots(13)$$

Birley[72] has noted that it is almost impossible to distinguish between γ-Fe_2O_3 (HFe_5O_8) and Fe_3O_4 by the electron diffraction technique because of the limitations in the accuracy of the technique.

5. SUMMARY

Polarization studies, slow strain rate tests, fracture mechanics tests, electron diffraction, and fractographic techniques have been employed to obtain engineering data and to reveal the mechanism of cracking of 316 stainless steel in caustic solutions.

In NaOH solution, cracking occurred in the primary transpassive potential range where the chromium passive film was unstable and dissolution of chromium to CrO_4^{2-} was occurring. At active-passive potentials, only sensitized material showed some susceptibility, and that may have resulted from film instability and iron dissolution. The mechanism of cracking at primary transpassive potentials in NaOH solution appeared to be dissolution, which may involve an adsorption step. There was evidence that diffusion in the liquid phase also affected cracking kinetics at potentials in the secondary passive region.

In the NaOH + Na_2S solutions, cracking occurred at active potentials. Film instability at these potentials

may have resulted from the presence of sulfide. Hydrogen embrittlement could not be ruled out at active-passive potentials.

BIBLIOGRAPHY

1. J. E. Truman and R. Perry, Brit. Corr. J. 1 pp.60-66 (1966).

2. P. P. Snowden, J.I.S.I. 197 pp. 136-141 (1961).

3. P. P. Snowden, J.I.S.I. 194 pp. 181-189 (1960)

4. A. J. Sedriks, S. Floreen and A. R. McIlree, Corrosion 32 pp. 157-158 (1976).

5. I. L. W. Wilson and R. G. Aspden, Corrosion 32 pp. 193-201 (1976).

6. A. R. McIlree and H. T. Michels, Corrosion 33 pp.60-67 (1977).

7. G. J. Theus, Nuclear Technology 28 pp. 388-397 (1976).

8. Y. S. Park, J. R. Galvele, A. K. Agrawal and R. W. Staehle Corrosion 34 pp.413-418 (1978).

9. Y. S. Park, A. K. Agrawal and R. W. Staehle in Extended Abstracts 76-1, The Electrochemical Society, Princeton (1976) pp. 109-111.

10. L. F. Lin, G. Cragnolino, Z. Szklarska-Smialowska and D. D. MacDonald, Corrosion 37 pp. 616-627 (1981).

11. Stress Corrosion Cracking : The Slow Strain Rate Technique STP 665 ed. G. M. Ugiansky and J. H. Payer, ASTM, Philadelphia (1979).

12. M. O. Speidel, Corrosion 32 pp. 187-190 (1976).

13. M. O. Speidel, Met. Trans. A. 12A pp. 779-789 (1981).

14. A. J. Russel and D. Tromans, Met. Trans. A 10A pp. 1229-1237 (1979).

15. A. J. Russel and D. Tromans, Met. Trans. A 12A pp. 613-621 (1981).

16. R. W. Staehle in The Theory of Stress Corrosion Cracking in Alloys, ed. J.C. Scully, NATO, Brussels pp. 223-288 (1971).

17. G. J. Theus and R. W. Staehle in Stress Corrosion Cracking and Hydrogen Embrittlement of Iron Base Alloys, ed. R. W. Staehle, J. Hochmann, R. D. McCright and J. E. Slater, NACE, Houston, pp. 845-891 (1977).

18. A J. Sedriks. Corrosion of Stainless Steels, J. Wiley and Son, Toronto (1979).

19. R. M. Latanision and R. W. Staehle in Fundamental Aspects of Stress Corrosion Cracking ed. R. W. Staehle, A. J. Forty, Houston, pp. 214-307 (1967).

20. H. E. Hänninen, International Met. Rev. 24 pp. 85-135 (1979).

21. R. W. Staehle in Stress Corrosion Cracking and Hydrogen Embrittlement of Iron Base Alloys, ed. R. W. Staehle, J. Hochmann, R. D. McCright and J. E. Slater, NACE, Houston, pp. 180-207 (1977).

22. A. K. Agrawal and R. W. Staehle in Stress Corrosion Cracking of Fe-Cr-Ni Alloys in Caustic Environments, The Ohio State University Research Foundation Report No. COO-2018-23 (Q-7) (1970) as quoted in Reference 17.

23. P. E. Morris in Extended Abstracts 76-1 The Electrochemical Society, Princeton, pp. 98-99 (1976).

24. L. Dahl, T. Dahlgren and N. Lagmyr in High Temperature High Pressure Electrochemistry in Aqueous Solutions, ed. R. W. Staehle, D. de G. Jones and J. E. Slater, NACE, Houston, pp. 533-545 (1976).

25. M. F. Long, A. K. Agrawal and R. W. Staehle in High Temperature High Pressure Electrochemistry in Aqueous Solutions, ed. R. W. Staehle, D. de G. Jones and J. E. Slater, NACE, Houston, pp. 524-531 (1976)

26. A. K. Agrawal, K. G. Sheth, K. Poteet and R. W. Staehle, J. Electrochem. Soc. 119 pp. 1637-1644 (1972).

27. H. Okada, S. Abe and T. Murata in Passivity and Its Breakdown on Iron and Iron Base Alloys, ed. R. W. Staehle and H. Okada, NACE, Houston, pp. 147-154 (1976).

28. I.L.W. Wilson, F. W. Pement and R. G. Aspden, Corrosion 34 pp. 311-320 (1978).

29. Y. S. Park, A. K. Agrawal and R. W. Staehle, Corrosion 35 pp. 333-339 (1979).

30. R. S. Shalvoy, S. K. Duglin and R. J. Lindinger Corrosion 37 pp. 491-497 (1981).

31. D. Singbeil and D. Tromans in Corrosion in the Pulp and Paper Industry - 1980 Symposium, NACE, Houston, in press.

32. W. A. Mueller in Pulp and Paper Industry Corrosion Problems V.2, NACE, Houston, pp. 140-146 (1977).

33. L. H. Laliberte in Pulp and Paper Industry Corrosion Problems V.2, NACE, Houston, pp. 1-11 (1977).

34. R. J. Asaro, Ph.D. Thesis, Stanford University (1972) as quoted in Reference 17.

35. V. P. Siderov and A. V. Ryabchenkov, Metallovedenie i Okrabotka Metallov 25 (1958) June as quoted in Reference 19.

36. H. R. Copson in Physical Metallurgy of Stress Corrosion Fracture, ed. T. N. Rhodin, Interscience, New York pp. 247-272 (1959).

37. H. H. Lee and H. H. Uhlig, J. Electrochem. Soc. 117 pp. 18-22 (1970).

38. K. L. Crooks and G.E. Linnert, TAPPI 44(8) pp. 544-554 (1961).

39. I. L. Wilson, F. W. Pement and R. G. Aspden, Corrosion 30 pp. 139-149 (1974).

40. A. R. McIlree, H. T. Michels and P. E. Morris, Corrosion 31 pp. 441-448 (1975).

41. W. M. Scott, Corrosion 17 (6) pp. 14-18 (1961).

42. W. A. Mueller in Pulp and Paper Industry Corrosion Problems, NACE, Houston, pp. 109-116 (1974).

43. A. J. Sedriks, J. Inst. Metals 101 pp. 225-232 (1973).

44. K. T. Aust, J. S. Armijo and J. H. Westbrook, A. S. M. Trans. Quart. 59 pp. 544-556 (1966).

45. I. L. W. Wilson and R. G. Aspden in Stress Corrosion Corrosion Cracking and Hydrogen Embrittlement of Iron Base Alloys, ed. R. W. Staehle, J. Hochmann, R. D. McCright and J. E. Slater, NACE, Houston, pp. 1189-1204 (1977).

46. E. N. Pugh in Stress Corrosion Cracking and Hydrogen Embrittlement of Iron Base Alloys, ed. R. W. Staehle, J. Hochmann, R. D. McCright and J. E. Slater, NACE, Houston pp. 37-51 (1977).

47. R. J. Asaro, A. J. West, and W. A. Tiller in Stress Corrosion Cracking and Hydrogen Embrittlement of Iron Base Alloys, ed. R. W. Staehle, J. Hochmann, R. D. McCright and J. E. Slater, NACE, Houston, pp. 1115-1124 (1977).

48. A. J. Russel, M. Sc. Thesis, University of British Columbia (1977).

49. D. Singbeil, M. Sc. Thesis, University of British Columbia (1981).

50. N. A. Nielsen, Corrosion 20 pp. 104t-110t (1964).

51. D. A. Vermilyea in Stress Corrosion Cracking and Hydrogen Embrittlement of Iron Base Alloys, ed. R. W. Staehle, J. Hochmann, R. D. McCright and J. E. Slater, NACE, Houston, pp. 208-217 (1977).

52. R. B. Diegle and D. A. Vermilyea, Corrosion 32 pp. 353-357 (1976).

53. J. C. Scully, Metal Sci. 12 pp. 290-300 (1978).

54. J. C. Scully, Corrosion Sci. 20 pp. 997-1016 (1980).

55. J. F. Newman, CERL Report RD/L/N 120/78 November (1978) as quoted in Reference 54.

56. G. J. Bignold, Corrosion 28 pp. 307-312 (1972).

57. P. Doig and P. E. J. Flewitt, Corrosion 37 pp. 378-383 (1981).

58. M. L. Holzworth, Corrosion 25 pp. 107-115 (1969).

59. R. N. O'Brien and P. Seto, J. Electrochem. Soc. 117 pp. 32-34 (1970).

60. M. Pourbaix, Lectures on Electrochemical Corrosion, Plenum, New York (1973).

61. D. Tromans, J. Electrochem. Soc. 127 pp. 1253-1256 (1980).

62. D. A. Wensley and R. S. Charlton, Corrosion 36 pp. 385-389 (1980).

63. D. Singbeil and D. Tromans, J. Electrochem. Soc. 128 pp. 2065-2070 (1981).

64. G. Cragnolino, L. F. Lin and Z. Szklarska-Smialowska, Corrosion 37 pp. 312-320 (1981).

65. J. F. Knott, Fundamentals of Fracture Mechanics, John Wiley and Sons, Toronto (1973).

66. ANSI/ASTM Standard E399-78a, ASTM, Philadelphia (1978).

67. B. F. Brown, Met. Rev. 13 pp. 171-183 (1968).

68. J. I. Dickson, A. J. Russel and D. Tromans, Can. Met Q. 19 pp. 161-167 (1980).

69. R. G. Stanton, Numerical Methods for Science and Engineering, Prentice-Hall, Englewood Cliffs (1961).

70. T. P. Nikiforuk, M.A.Sc. Thesis, University of British Columbia (1976).

71. ASTM Powder Diffraction File-Card No. 11-614 for Fe_3O_4.

72. S. Birley, Ph.D. Thesis, University of British Columbia (1972).

73. J. B. Lee, Corrosion 37 pp. 467-481 (1981).

74. R. L. Cowan and R. W. Staehle, J. Electrochem. Soc. 118 pp. 557-568 (1971).

75. R. J. Biernat and R. G. Robins, Electrochim Acta 17 pp. 1261-1283 (1972).

76. R. J. Biernat and R. G. Robins, Electrochim Acta 14 pp. 809-820 (1969).

77. D. D. MacDonald and B.C. Syrett, Corrosion 35 pp. 471-475 (1979).

78. G. Santarini and J. Y. Boos, Corrosion Sci. 19 pp. 261-281 (1979).

79. B. J. Berkowitz and H. H. Horowitz, J. Electrochem. Soc. 129 pp. 468-474 (1982).

80. R. N. Parkins in Stress Corrosion Cracking and Hydrogen Embrittlement of Iron Base Alloys ed. R. W. Staehle, J. Hochmann, R. D. McCright and J. E. Slater, NACE, Houston pp. 601-619 (1977).

81. T. P. Hoar and R. W. Jones, Corrosion Sci. 13 pp. 725-738 (1973).

82. R. B. Diegle and D. A. Vermilyea, J. Electrochem. Soc. 122 pp. 180-188 (1975).

83. J. M. West, Electrodeposition and Corrosion Processes, D. van Nostrand, London (1965).

84. T. Murata and R. W. Staehle, unpublished results as quoted by R. W. Staehle in The Theory of Stress Corrosion Cracking in Alloys ed. J. C. Scully, NATO, Brussels (1971) pp. 223-288.

85. T. P. Hoar, Fundmanetal Aspects of Stress Corrosion Cracking ed. R. W. Staehle, A. J. Forty and D. van Rooyen, NACE, Houston, pp. 98-103 (1969).

86. M. C. Petit, Electrochim. Acta 13 pp. 557-569 (1968).

87. R. S. Sapieszko and E. Matijevic, Corrosion 37 pp. 152-161 (1981).

88. P. Taylor and D. W. Shoesmith, Can. J. Chem. 56 pp. 2797-2802 (1978).

89. N. Bandyopadhyay and C. L. Briant, Corrosion 38 pp. 125-129 (1982).

90. R. Knoedler and K. E. Heusler, Electrochim. Acta 17 pp. 197-212 (1972).

91. E. J. W. Verwey and E. L. Heilmann, J. Chem. Phys. 15 pp. 174-180 (1947).

92. M. C. Bloom and L. Goldenberg, Corrosion Sci. 5 pp. 623-630 (1965).